Develop and Implement a Phase-field-based Model for Brittle Fracture

by

Hung Cuong NGUYEN

THESIS PRESENTED TO ÉCOLE DE TECHNOLOGIE SUPÉRIEURE
IN PARTIAL FULFILLMENT OF A MASTER'S DEGREE
WITH THESIS IN MECHANICAL ENGINEERING
M.A.Sc.

MONTREAL, "JUNE 28TH, 2024"

ÉCOLE DE TECHNOLOGIE SUPÉRIEURE
UNIVERSITÉ DU QUÉBEC

BOARD OF EXAMINERS

THIS THESIS HAS BEEN EVALUATED

BY THE FOLLOWING BOARD OF EXAMINERS

Mr. Tan Pham, Thesis supervisor
Département de Génie Mécanique, École de Technologie Supérieure

Mr. Ricardo Zednik, Chair, Board of Examiners
Département de génie mécanique, École de Technologie Supérieure

Mr. Raynald Guilbault , Member of the Jury
Département de Génie Mécanique, École de Technologie Supérieure

THIS THESIS WAS PRESENTED AND DEFENDED

IN THE PRESENCE OF A BOARD OF EXAMINERS AND THE PUBLIC

ON "MAY 29TH, 2024"

AT ÉCOLE DE TECHNOLOGIE SUPÉRIEURE

ACKNOWLEDGEMENTS

Développer et Réaliser un Modèle Basé sur le Champ de Phase pour la Rupture Fragile

Hung Cuong NGUYEN

RÉSUMÉ

Les objectifs de cette thèse, composée de quattre chapitres, sont de développer et de mettre en œuvre un modèle de champ de phase pour la rupture fragile en condition de contrainte plane. **Chapitre 1** présente brièvement la motivation et les objectifs du projet. **Chapitre 2** discute de la revue de la littérature sur la mécanique de la rupture, depuis l'idée de Griffith d'équilibre énergétique autour de la fissure, jusqu'à la méthode des éléments finis étendus (XFEM), et enfin la plus récente tendance dans le domaine, le modèle de champ de phase pour la rupture. **Chapitre 3** illustre les fondements mathématiques du modèle de champ de phase pour la rupture fragile et comment l'introduire dans le cadre des éléments finis en utilisant une approche variationnelle. **Chapitre 4** propose deux nouveaux développements au modèle actuel: *le changement du comportement des matériaux pour la condition de contrainte plane* et *le schéma adaptatif échelonné* pour améliorer la convergence du solveur d'éléments finis. Ensuite, les résultats de deux expériences numériques sont analysés pour valider le cadre. Enfin, la conclusion donne un bref résumé et des recommandations pour les travaux futurs.

Mots-clés: rupture fragile, modèle de champ de phase, condition de contrainte plane, algorithme décalé, méthode des éléments finis

Develop and Implement a Phase-field-based Model for Brittle Fracture

Hung Cuong NGUYEN

ABSTRACT

This thesis aims to develop and implement a phase-field model for brittle fracture in plane stress condition. It is composed of four themed chapters. Firstly, **Chapter 1** introduces the motivation and objectives of the project. The lack of an effective simulation tool in predicting the cracks that usually occur in thin objects motivates the author to *develop a mathematical model that could capture their fracture mechanism*. **Chapter 2** begins by laying out the theoretical dimensions of the research and provides a brief review of fracture models, initiating from the classical *Linear Elastic Fracture Model* to phenomenally effective implementation of crack growth, *Extended finite element method* (XFEM), and ending up with the state-of-the-art approach, namely *phase-field model for fracture*. Next, **Chapter 3** revisits the theory behind the phase-field model for fracture, its finite element formulation, and some notable variations. **Chapter 4** presents two new developments, including the *adaptive staggered scheme*, to the original framework in the theory part and then analyzes the results of numerical experiments applying these adjustments. Finally, the conclusion gives a brief summary and recommendations for future work.

Keywords: phase-field model, brittle fracture, staggered algorithm, plane stress condition, finite element method

TABLE OF CONTENTS

XII

LIST OF TABLES

LIST OF FIGURES

LIST OF ALGORITHMS

LIST OF ABBREVIATIONS

ETS   École de Technologie Supérieure

FEM   Finite Element Method

XFEM   Extended Finite Element Method

LEFM   Linear Elastic Fracture Mechanics

CZM   Cohesive Zone Model

PFM   Phase Field Model

PDE   Partial Differential Equation

dof   Degree of freedom

LIST OF SYMBOLS AND UNITS OF MEASUREMENTS

$\mathbf{b}$	Body force
$\mathbb{C}$	Fourth-order constitutive tensor for linear elasticity
$\mathbf{C}$	Second-order constitutive tensor for linear elasticity
E	Young's modulus
$E(\mathbf{u}, \Gamma)$	Free energy as a function of displacement and sharp crack
$E(\mathbf{u}, c)$	Free energy as a function of displacement and crack field
E^u	Elastic strain energy
E^c	Surface energy
$\mathbf{f}_{int}^e$	Internal element force vector
$\mathbf{f}_{ext}^e$	Eternal element force vector
$\mathbf{f}_{int}$	Internal global force vector
$\mathbf{f}_{ext}$	Eternal global force vector
$\bar{\mathbf{f}}, \bar{\mathbf{f}}_p$	Reaction force vector corresponding to prescribed displacement
G	Shear modulus
G_c	Critical energy release rate
$\mathbb{I}^s$	Symmetric fourth-order unit tensor $\mathbb{I}^s = \frac{1}{2}(\delta_{ik}\delta_{jl} + \delta_{il}\delta_{jk})$
$\mathbf{I}$	Second-order unit tensor
K	Bulk modulus
$\mathbf{K}^u$	Tangent stiffness matrix for displacement

$\mathbf{K}^c$	Tangent stiffness matrix for crack field
l	Characteristics length scale
nGp	Number of Gauss points used in the calculation of the integral
$\mathbf{r}^u$	Residual of displacement field
$\mathbf{r}^c$	Residual of crack field
$\mathbf{r}_p$	Residual of prescribed displacement
$\mathbf{r}_f$	Residual of free displacement
$\mathbf{t}^*$	Traction force in Neumann's boundary condition
W	The external potential energy applies to a solid
ν	Poisson's ratio
μ	Lamé parameter
λ	Lamé parameter
$\boldsymbol{\sigma}$	Stress tensor
$\boldsymbol{\epsilon}$	Strain tensor
Γ	A sharp crack occurred in the solid
Γ_l	A smeared crack zone replaces the sharp crack in the solid
Π	The total energy functional of a solid
Ψ	Elastic energy density
Ω	Domain of a solid
$\partial\Omega$	Boundary of solid Ω

$\partial\Omega_D$ Domain of Dirichlet's boundary conditions

$\partial\Omega_N$ Domain of Neumann's boundary conditions

$\nabla^s(\cdot)$ Symmetric divergence operator, $\nabla^s(\cdot) = \frac{1}{2}(\nabla(\cdot) + \nabla^T(\cdot))$

$\delta\Pi$ Variation of total energy

$\delta\mathbf{u}$ Variation of displacement

δc Variation of crack

δE Variation of free energy

$\delta_u E$ Variation of free energy with respect to $\mathbf{u}$ (displacement)

$\delta_c E$ Variation of free energy with respect to c (crack field)

INTRODUCTION

The fracture behavior of materials is one of the most essential topics in engineering practice and design. Preventing structure from crack-inflicted failure is always the utmost priority in any mechanical design concept. Thus, a computational model that can predict the fracture process within the structures would be an invaluable tool in this regard. During the entire history of fracture mechanics, developing a fracture model that is a well-self-contained feature, i.e., can automatically open the crack and then follow its trajectory, is one of the most challenging jobs. The recent trend in the phase-field-based fracture model allows us to build such a tool. The objective of this master thesis is two-fold:

- To develop and implement the *phase-field model for brittle fracture in the plane stress state*.
- To introduce an *adaptive staggered scheme* that could automatically adjust the load ratio in compliance with the energetic stability of the system.

CHAPTER 1

OBJECTIVES

1.1   Phase-field model for brittle fracture in the plane stress state

While implementing a phase-field model in two-dimensional (2D) attracts great interest in computational mechanics due to its feasibility in terms of computational cost, they are dominantly in plane strain state. The plane stress condition, which is better suited for thin, planar, and crack-prone solids, has yet to be fully analyzed to couple with the crack fields. All of these facts lead to the first objective of this work, which is to develop a *phase field-based fracture model in plane stress mode*.

1.2   Adaptive staggered scheme

At the very core of the phase-field-based fracture model, crack propagation is the result of minimizing the solids' energy potential, consisting of elastic and surface energy. When the elastic energy, which comes from the elastic deformation caused by the external load, reaches a critical value, the minimization constraint lowers it by increasing the crack field, which raises the surface energy. The staggered algorithm, which solves the displacement and crack field separately, mathematically guarantees it by finding the solution of two linear equation systems. However, one of the most challenging tasks of the staggered scheme is to keep it in the convergence zone when the solid is about to open a crack. It is because the energy potential drastically increases and becomes volatile, i.e., it exponentially fluctuates away from the stability balance between its two components at that point. The second objective of this thesis is to propose a new approach to implement the original algorithm to overcome this issue.

<center>**CHAPTER 2**</center>

<center>**LITERATURE REVIEW**</center>

2.1   Early research on fracture mechanics

Fracture mechanics is an important element within the engineering domain, but its origin only started in the wake of The Liberty Ships' failure during World War II. The breakdown of their failure, reported by Williams, Ellinger *et al.* (1953), pointed to local stress concentration caused by the flawed welded joints. In addition, the poor toughness of the steel partially contributed to these failures. From the foundation work of Griffith & Taylor (1921) and others, Irwin (1956) of the Naval Research group introduced one the most essential concept of fracture analysis, the *energy release rate G*, which represents the rate of transforming potential energy into fracture surface area. Mathematically, given a solid with total energy functional Π and unit crack growth area Γ, $G \equiv -\frac{\partial \Pi}{\partial \Gamma}$. At the moment the energy release rate G reaches its threshold value G_c, the critical energy release rate by the unit of J/m^2, the crack occurs. G_c is a material property representing its toughness against fracture. Later on, the Linear Elastic Fracture Mechanics (LEFM) framework proposed by Irwin (1957) used the concept namely *stress-intensity factors* to analyze the stress distribution near crack-tip.

Despite variable successful application on linear elastic material, LEFM failed when plastic deformation arose prior to the failure of the material. Rice (1968) proposed a method to calculate the J-integral, a global parameter that characterizes the crack tip criteria and could judge the reliability of a pre-defining crack. The approach quickly became the standard measure of fracture toughness, with the experiment conducted by Begley & Landes (1972). Besson (2010) indicated some minuses of this method; for example, it cannot automatically initiate and propagate the crack from an existing notch or a point that possesses a high-stress intensity; the threshold of the J-integral is not a specific material characteristic because it heavily depends on the geometric shape of the specimen, and thus it could hardly apply for any arbitrarily complex geometry. Another model is proposed by Gurson (1977) in which the plastic flow relies on a damage parameter induced by void volume porosity. Its revised version, Gurson-Tvergaard-Needleman

(GTN) model by Tvergaard & Needleman (1984), assimilates some parameters to designate the void growth kinetics. Their fatal disadvantage is the strong dependency on the mesh size of the results because the damage level dramatically affects the softening mechanism.

2.2   Extended Finite Element Method and Cohesive Zone Model

The finite element method (FEM), cf. Zienkiewicz, Taylor & Fox (2014), is one of the most widely used numerical methods in both the research and engineering communities. However, it faces a huge challenge in dealing with discontinuities due to the nature of the variational method, which requires continuity values in the domain of interest. *Extended Finite Element Method* (XFEM), cf. Moës, Dolbow & Belytschko (1999); Moës, Stolz, Bernard & Chevaugeon (2011), enables the possibility to track the discontinuities within existing mesh by means of a level set function. However, all crack-related processes, such as crack initiation and crack propagation, need to be pre-defined in constitutive equations. More complicated issues, such as crack branching, is either unlikely to be captured or significantly difficult to implement.

Another interesting method, namely *Cohesive Zone Model* (CZM), which is originally proposed by Barenblatt (1962), develops a virtual element to describe the crack mechanism through an interface between crack-free and cracked regions, cf. Xu & Needleman (1994). An isogeometric implementation of this model, conducted by Dimitri, De Lorenzis, Wriggers & Zavarise (2014), explicitly defined the fracture process zone and thus led the prescribed crack paths in a straightforward manner. Attempts to propagate crack path require an additional phenomenological cohesive element that strongly depends on mesh, thus overestimating the role of cracked areas.

Despite success in tracking the evolution of crack, the introduction of discontinuities into standard finite element of continuous solid by using either *cohesive surfaces* in CZM, cf. Ortiz & Pandolfi (1999), or *enriched finite element* in XFEM, cf. Simo, Oliver & Armero (1993) still requires additional criteria for the crack to grow and propagate in the solid.

2.3   Phase-field model for fracture

The phase-field model for fracture is an energy-based framework that could naturally incorporate the crack discontinuities into finite element formulation by using a variational approach. Originated from the theory work of Griffith & Taylor (1921), the crack surface energy term in a solid's energy potential is then regularized from the crack surface into the whole approximation domain, cf. Bourdin, Francfort & Marigo (2000, 2008), thanks to the mathematical development on the variational approach to brittle fracture of Francfort & Marigo (1998) and $\Gamma-$convergence theorem of Braides (1998). This regularized formulation has two crucial elements: a sharp crack to be smeared out into an additional crack field c and the *stress degradation function*, which connects the crack field with the stress-strain relationship. Series of research from Amor, Marigo & Maurini (2009); Miehe, Hofacker & Welschinger (2010b); Miehe, Welschinger & Hofacker (2010a); Kuhn & Müller (2010); Borden, Verhoosel, Scott, Hughes & Landis (2012) confirms the advantages of this approach:

- Efficiently handle complex fracture behaviors, e.g. crack initiation, propagation, and branching, without any additional criteria.
- The evolution of the crack is automatically tracked at each load step without the re-mesh requirement.
- Implementation is straightforward, even with multi-dimensional and multi-physics cases.

In terms of solving strategy, although the monolithic solver, which solves displacement and crack field simultaneously, is faster, it is numerically unstable. Several techniques are proposed to that end, including Gerasimov & De Lorenzis (2016) for line search technique; Msekh, Sargado, Jamshidian, Areias & Rabczuk (2015) of additional penalty term; or Heister, Wheeler & Wick (2015) of the primal-dual scheme. The *staggered algorithm*, first proposed by Amor *et al.* (2009), on the other hand, solves the two fields separately. It heavily dominates most of the implementation of the phase-field model due to its robustness and stability.

CHAPTER 3

THEORY UNDERLYING THE PHASE-FIELD MODEL FOR FRACTURE

3.1   Phase-field approximation of the sharp crack

The key idea of the phase-field model is simple: replace the sharp crack, which represents the discontinuity, by a crack field value, which varies from value 0 indicating intact state to 1 meaning fully broken. Figure 3.1 illustrates the result of stretching out of sharp crack Γ into crack phase-field value c within an area framed by the *characteristic length l*.

a) Sharp crack   b) Smeared crack
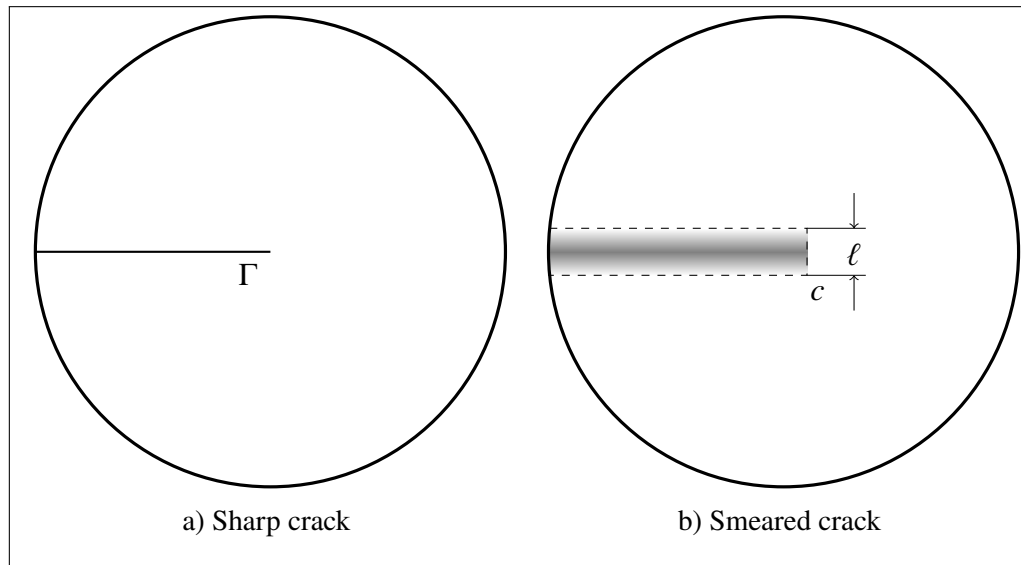
Figure 3.1   Sharp crack Γ (a) is stretched to a continuous
graded area (b) controlled by length scale l

In the one-dimensional (1D) case, assuming that a sharp crack existed at $x = 0$, Miehe *et al.* (2010a) proposed the form of its diffused representation as

$$c(x) = \exp\left(-\frac{|x|}{\ell}\right) \tag{3.1}$$

which fulfills the boundary conditions

$$\begin{cases} c(x) = 1 & \text{when } x = 0 \\ c(x) \to 0 & \text{when } x \to \pm\infty \end{cases} \tag{3.2}$$
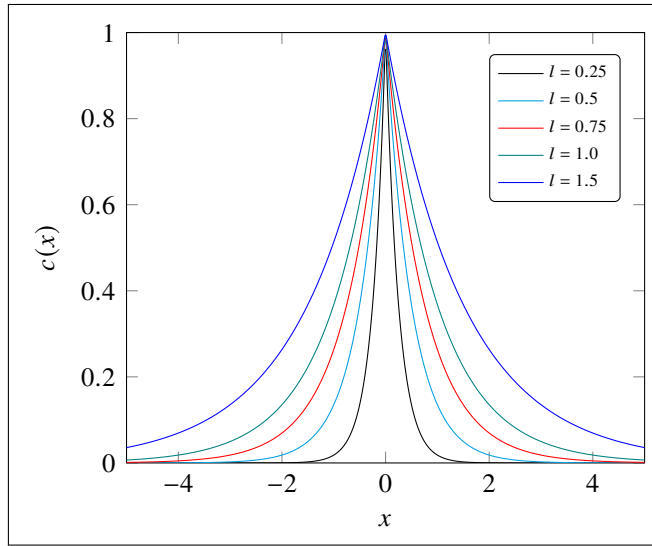
Figure 3.2   Effect of length scale l on the distribution of
smeared crack $c(x)$ when a sharp crack occurs at $x = 0$ in 1D

From a mathematical view, the form of $c(x)$ in eq.(3.1) is the solution of this differential equation

$$c(x) - \ell^2 c''(x) = 0 \tag{3.3}$$

The general solution of equation (3.3) is the result of minimizing the *crack surface density functional*

$$\Gamma_\ell(c) = \frac{1}{2\ell} \int_\Omega \left(c^2 + \ell^2 (c')^2 \right) dx \tag{3.4}$$

With the assistance of the $\Gamma-$ convergence theorem, cf. Braides (1998), its extension to multi-dimensional case reads

$$\Gamma_\ell(c) = \frac{1}{2\ell} \int_\Omega \left(c^2 + \ell^2 |\nabla c|^2 \right) d\mathbf{x} \tag{3.5}$$

3.2 Phase-field model for brittle fracture

This section aims to construct the finite element framework from the minimum energy principle of solids. The following steps are carried out in order to reach that goal:

- *To minimize* the total energy functional.
- *To derive* the governing equations in the *strong form* from the minimization process.
- *To transform* the strong form into the *weak form*.
- *To discretize* the solid into finite elements, *assemble* the residual between the external and internal forces, and then *linearize* the residual to obtain the linear system.
- To introduce the *staggered algorithm* as a solver for the framework.

3.2.1 Total energy functional of fractured solid and its minimization

Given a solid Ω, constrained by the Dirichlet's boundary condition on $\partial\Omega_D$, with a crack Γ occurred due to external loads. Its total energy functional Π consists of the *free energy functional* $E(\mathbf{u}, \Gamma)$ and the *external potential energy* W, produced by the external loads:

$$\Pi = E(\mathbf{u}, \Gamma) - W$$

The external potential energy W is defined as the total work of both the body forces $\mathbf{b}$ over the whole domain Ω and the traction forces $\mathbf{t}^*$ over the surface applied (on the boundary $\partial\Omega_N$ in this case) that caused the displacement $\mathbf{u}$ of the solid:

$$W = \int_\Omega \mathbf{b} \cdot \mathbf{u} \, dV + \int_{\partial\Omega_N} \mathbf{t}^* \cdot \mathbf{u} \, dA$$

The free energy functional comprises the *elastic strain energy E^u* induced by the displacement **u**, and the *surface energy E^c* released by the opening of the crack Γ. It is worth noting that the calculation of E^u must exclude the crack surface Γ due to the discontinuity of **u** in that region.

$$E(\mathbf{u}, \Gamma) = \underbrace{\int_{\Omega\backslash\Gamma} \Psi(\epsilon) dV}_{E^u} \quad + \quad \underbrace{\int_{\Gamma} G_c \, dA}_{E^c} \tag{3.6}$$

In linear elasticity, $\Psi(\epsilon)$ is called as the *elastic energy density $-\Psi(\epsilon) \equiv \frac{1}{2}\lambda\mathrm{tr}^2(\epsilon) + \mu(\epsilon : \epsilon)$* where μ, λ are the Lamé parameters. The *critical energy release rate $- G_c$* is a measure of the material's fracture toughness.

To deal with the discontinuity in equation (3.6), Bourdin *et al.* (2008) used the variational form of the smeared crack defined in equation (3.5) to regularize the sharp crack Γ into the whole domain Ω. As a result, the surface energy in that area is also spread out to the whole domain and becomes the *surface energy functional*. With this regularized form in place, the crack field c, which varies from value 0 of the intact state to 1 of a fully broken one, is added as an additional degree of freedom (dof) at each node, representing its level of damage. In addition, the *stress degradation function* introduced in the strain energy reflects the crack field's effect on the solid's mechanical response. In terms of energy, the crack initiation and propagation process is driven by the energetic battle between the strain energy in the solid and the surface energy produced by the crack field.

$$\begin{aligned} E(\mathbf{u}, c) &= \int_\Omega g(c)\Psi(\epsilon)dV + \int_\Omega G_c \Gamma_l \, dV \\ &= \underbrace{\int_\Omega g(c)\Psi(\epsilon)dV}_{E^u} + \underbrace{\int_\Omega \frac{G_c}{2}\left(\frac{c^2}{l} + l|\nabla c|^2\right) dV}_{E^c} \end{aligned} \tag{3.7}$$

where $g(c) \equiv (1 - c)^2$ *– the stress degradation function*

The admissible solution for the displacement field and crack field then comes down to the energetic minimization of the total energy functional Π, i.e. its first variation $\delta\Pi$ must vanish.

$$(\mathbf{u}, c) = \arg\min\left\{\Pi(\mathbf{u}, c)\right\}$$

The details on calculation of $\delta\Pi$ are as follows:

$$\delta\Pi = \delta E - \delta W, \quad \text{in which} \quad \begin{cases} \delta W = \int_\Omega \mathbf{b} \cdot \delta\mathbf{u}\, dV + \int_{\partial\Omega_N} \mathbf{t}^* \cdot \delta\mathbf{u}\, dA \\[2mm] \delta E = \delta_u E + \delta_c E \end{cases}$$

The side calculation of δE includes these steps:

· *To calculate the variation of free energy with respect to displacement*

$$\delta_u E \equiv \frac{\partial E}{\partial\boldsymbol{\epsilon}} : \delta\boldsymbol{\epsilon} = \int_\Omega \frac{\partial[g(c)\Psi(\boldsymbol{\epsilon})]}{\partial\boldsymbol{\epsilon}} : \delta\boldsymbol{\epsilon}\, dV = \int_\Omega \boldsymbol{\sigma} : \delta\boldsymbol{\epsilon}\, dV$$

$$= \int_{\partial\Omega} (\boldsymbol{\sigma} \cdot \mathbf{n}) \cdot \delta\mathbf{u}\, dS - \int_\Omega \text{div}\boldsymbol{\sigma} \cdot \delta\mathbf{u}\, dV \ \text{(using divergence theorem)}$$

· *To apply the divergence theorem on $\delta_c E$*

$$\nabla \cdot (\delta c \nabla c) = \nabla c \cdot \nabla\delta c + \delta c\, \triangle c \quad \Rightarrow \quad \nabla c \cdot \nabla\delta c = \nabla \cdot (\delta c \nabla c) - \delta c\, \triangle c$$

$$\xRightarrow[\text{theorem}]{\text{Divergence}} \int_\Omega (\nabla c \cdot \nabla\delta c)\, dV = \int_{\partial\Omega} \delta c\, \nabla c \cdot \mathbf{n}\, dS - \int_\Omega \delta c\, \triangle c\, dV$$

· *To calculate the variation of free energy with respect to crack field*

$$\delta_c E \equiv \frac{\mathrm{d}}{\mathrm{d}\alpha} E(c + \alpha\delta c)\Big|_{\alpha=0} \ \text{(Gateaux derivative)}$$

$$= \int_\Omega \frac{\partial[g(c)\Psi(\boldsymbol{\epsilon})]}{\partial c} \cdot \delta c\, dV + \frac{G_c}{2} \int_\Omega \left(\frac{\partial}{\partial c}\left[\frac{c^2}{l}\right] \cdot \delta c + \frac{\partial[l\,\nabla c \cdot \nabla c]}{\partial\nabla c} \cdot \nabla\delta c\right) dV$$

$$= \int_\Omega g_{,c}\Psi \cdot \delta c\, dV + G_c \int_\Omega \left(\frac{c}{l}\delta c + l\,\nabla c \cdot \nabla\delta c\right) dV$$

$$= \int_\Omega g_{,c}\Psi \cdot \delta c\, dV + G_c \int_\Omega \left(\frac{c}{l} - l\,\triangle c\right) \cdot \delta c\, dV + \int_{\partial\Omega} \delta c\, (\nabla c \cdot \mathbf{n})\, dS$$

Finally, $\delta\Pi$ has the following form

$$\delta\Pi = \int_{\partial\Omega_N} (\boldsymbol{\sigma}\cdot\mathbf{n} - \mathbf{t}^*)\cdot\delta\mathbf{u}\ dS - \int_\Omega (\text{div}\boldsymbol{\sigma} + \mathbf{b})\cdot\delta\mathbf{u}\ dV +$$

$$+ \int_\Omega \left[G_c\left(-l\triangle c + \frac{c}{l}\right) + g_{,c}\Psi\right]\cdot\delta c\ dV + \int_{\partial\Omega} \delta c\ (\nabla c\cdot\mathbf{n})\ dS \qquad (3.8)$$

The fact that $\delta\Pi$ must vanish for all admissible $\delta\mathbf{u}$ and δc leads to a pair of partial differential equations (PDEs) for the displacement field $\mathbf{u}$ and crack field c.

3.2.2 Strong formulation

A finite element model's strong form can be obtained from minimizing its total energy functional. In this case, we start from the equation (3.8)

$$\delta\Pi = 0 \quad \forall \text{admissible } (\delta\mathbf{u}, \delta c) \quad \Rightarrow \quad \begin{cases} \boldsymbol{\sigma}\cdot\mathbf{n} - \mathbf{t}^* = \mathbf{0} & \text{on } \partial\Omega_N \\[2mm] \text{div}\boldsymbol{\sigma} + \mathbf{b} = \mathbf{0} & \text{in } \Omega \\[2mm] G_c\left(-l\triangle c + \frac{c}{l}\right) + g_{,c}\Psi = 0 & \text{in } \Omega \\[2mm] \nabla c\cdot\mathbf{n} = 0 & \text{on } \partial\Omega \end{cases}$$

Without loss of generality, the body force $\mathbf{b}$ is deemed zero in the displacement equilibrium equation. As a result, the traction $\mathbf{t}^*$ of Neumann's boundary condition is the only external source applying on the boundary of the solid.

$$\text{div}\boldsymbol{\sigma} = \mathbf{0} \qquad \text{in } \Omega \qquad\qquad (3.9)$$

$$\boldsymbol{\sigma}\cdot\mathbf{n} = \mathbf{t}^* \qquad \text{on } \partial\Omega_N \qquad\qquad (3.10)$$

The regularized equation of the crack phase-field reads

$$\frac{c}{l} - l\triangle c = \frac{2(1-c)}{G_c}\Psi \qquad \text{in } \Omega \qquad\qquad (3.11)$$

$$\nabla c\cdot\mathbf{n} = \mathbf{0} \qquad\qquad \text{on } \partial\Omega \qquad\qquad (3.12)$$

3.2.3 Weak formulation and discretization

The weak form provides a direction in which the two PDEs could be numerically solved because solving them directly in their strong forms is impractical. The transformation into the weak form of displacement field uses the weighted residual method, which can be found in any standard textbook about the finite element method, such as Zienkiewicz *et al.* (2014). Its weak form is to find $\mathbf{u} \in \mathcal{U}_u \equiv \{\mathbf{u} \,|\, \mathbf{u}(\mathbf{x}) = \mathbf{0} \ \forall \mathbf{x} \in \partial\Omega_D\}$ such that

$$\int_\Omega \boldsymbol{\sigma} : \nabla^s \delta\mathbf{u} \, dV = \int_{\partial\Omega_N} \mathbf{t}^* \cdot \delta\mathbf{u} \, dS \qquad \forall \delta\mathbf{u} \in \mathcal{V}_u \equiv \{\delta\mathbf{u} \,|\, \delta\mathbf{u}(\mathbf{x}) = \mathbf{0} \ \forall \mathbf{x} \in \partial\Omega_D\} \qquad (3.13)$$

Similarly, the weak form of the crack field is to find $c \in \mathcal{U}_c \equiv \{c \,|\, c(\mathbf{x}) \in [0, 1], \ \dot{c}(\mathbf{x}) \geq 0 \ \forall \mathbf{x} \in \Omega\}$ such that

$$\int_\Omega \left(2(c-1)\Psi \, \delta c + G_c \left[\frac{c}{l} \delta c + l\nabla c \cdot \nabla\delta c \right] \right) dV = 0 \qquad \forall \delta c \in \mathcal{V}_c \qquad (3.14)$$

$$\text{where } \mathcal{V}_c \equiv \{\delta c \,|\, \delta c(\mathbf{x}) \geq 0 \ \forall \mathbf{x} \in \Omega\}$$

The weak form in equation (3.13) allows discretizing the domain Ω into a finite of elements Ω^e in which the internal and external forces can be calculated as follows:

$$\mathbf{f}^e_{int} = \int_{\Omega^e} \mathbf{B}_u^T \boldsymbol{\sigma} \, dV$$

$$\mathbf{f}^e_{ext} = \int_{\partial\Omega_N^e} \mathbf{N}_u^T \mathbf{t}^* \, dS$$

After assembling global internal and external forces, the residual displacement field reads

$$\mathbf{r}^u \equiv \mathbf{f}_{int}(\mathbf{u}) - \mathbf{f}_{ext} = \mathbf{0} \qquad (3.15)$$

In the same manner, the residual of the crack field is constructed from the equation (3.14)

$$\mathbf{r}^c \equiv \int_\Omega \left(lG_c \mathbf{B}_c^T \nabla c + (\frac{G_c}{l} + 2\Psi)\mathbf{N}c - 2\Psi\mathbf{N}^T \right) dV = \mathbf{0} \qquad (3.16)$$

3.2.4 Linearization and Newton-Raphson scheme

As of this step, finding the solution $(\mathbf{u}, \mathbf{c})$ relies on solving the following system of equations:

$$\begin{cases} \mathbf{r}^u = \mathbf{0} \\ \mathbf{r}^c = \mathbf{0} \end{cases} \tag{3.17}$$

In general, both $\mathbf{r}^u = \mathbf{0}$ and $\mathbf{r}^c = \mathbf{0}$ are nonlinear systems that require the linearization process from the Newton-Raphson scheme to solve. Let us assume that the system enters a new load step in the incremental loading scheme. The residual for the displacement and crack field at step $k + 1$ are approximated by their values at step k in a typical Newton-Raphson loop, that is

$$\mathbf{r}^u(\mathbf{u}^{k+1}) \approx \mathbf{r}^u(\mathbf{u}^k) + \left.\frac{\partial \mathbf{r}^u}{\partial \mathbf{u}}\right|_k \delta \mathbf{u}^k = \mathbf{0} \quad \Rightarrow \quad \mathbf{K}^u_{|_k} \delta \mathbf{u}^k = -\mathbf{r}^u(\mathbf{u}^k) \tag{3.18}$$

$$\mathbf{r}^c(\mathbf{c}^{k+1}) \approx \mathbf{r}^c(\mathbf{c}^k) + \left.\frac{\partial \mathbf{r}^c}{\partial \mathbf{c}}\right|_k \delta \mathbf{c}^k = \mathbf{0} \quad \Rightarrow \quad \mathbf{K}^c_{|_k} \delta \mathbf{c}^k = -\mathbf{r}^c(\mathbf{c}^k) \tag{3.19}$$

$$\text{where} \quad \mathbf{K}^u \equiv \frac{\partial \mathbf{r}^u}{\partial \mathbf{u}} = \int_\Omega \mathbf{B}^T \left(\frac{\partial \boldsymbol{\sigma}}{\partial \boldsymbol{\epsilon}}\right) \mathbf{B} \, dV \tag{3.20}$$

$$\text{and} \quad \mathbf{K}^c \equiv \frac{\partial \mathbf{r}^c}{\partial \mathbf{c}} = \int_\Omega \left(G_c l (\mathbf{B}^c)^T \mathbf{B}^c + (\frac{G_c}{l} + 2\Psi)\mathbf{N}\mathbf{N}^T\right) dV \tag{3.21}$$

In this framework, the displacement-controlled loading scheme replaces the load-controlled scheme to capture the drop in the load-displacement curve after the crack occurs. A non-zero *prescribed displacement* $\bar{\mathbf{u}}$, which is repeatedly applied at each load step, replaces the traditional traction forces $\mathbf{t}^*$. This prescribed Dirichlet boundary conditions applied on the surface of the solid trigger unknown Neumann-like boundary condition values. It could be physically considered as reaction forces in stress analysis and only exists where prescribed displacement $\bar{\mathbf{u}}$ is placed. The following development offers the blueprint for the Newton-Raphson loop when changing the loading scheme. The objective is to establish the linear system that solves the displacements' increments and the reaction forces at the area prescribed displacement is applied.

Equation (3.15) can be split as follows:

$$
\begin{cases}
\mathbf{r}_p^u \equiv \mathbf{f}_p^{int} + \bar{\mathbf{f}}_p = \mathbf{0}, & p = 1...\bar{p} - \text{prescribed dofs} \\[2mm]
\mathbf{r}_f^u \equiv \mathbf{f}_f^{int} = \mathbf{0}, & f = \bar{p} + 1...N - \text{free dofs}
\end{cases}
\tag{3.22}
$$

Subscript p, which denotes *prescribed displacement*, represents the rows containing degree of freedom (dof) of $\bar{\mathbf{u}}$ while f stand for *free displacement* of the remaining dofs and $\bar{\mathbf{f}}$ is the corresponding reaction force with respect to $\bar{\mathbf{u}}$. Linearization of equation (3.22) requires applying Taylor expansion for both $\mathbf{r}_p(\bar{\mathbf{u}}, \mathbf{u}^f)$ and $\mathbf{r}_f(\bar{\mathbf{u}}, \mathbf{u}^f)$

$$
\mathbf{r}_p^{k+1}(\bar{\mathbf{u}}, \mathbf{u}^f) \approx \mathbf{r}_p^k + \left(\frac{\partial \mathbf{f}_p^{int}}{\partial \bar{\mathbf{u}}} \bigg|_k \right) \delta\bar{\mathbf{u}} + \left(\frac{\partial \mathbf{f}_p^{int}}{\partial \mathbf{u}^f} \bigg|_k \right) \delta\mathbf{u}^f + \left(\frac{\partial \bar{\mathbf{f}}_p}{\partial \bar{\mathbf{u}}} \bigg|_k \right) \delta\bar{\mathbf{u}} + \left(\frac{\partial \bar{\mathbf{f}}_p}{\partial \mathbf{u}^f} \bigg|_k \right) \delta\mathbf{u}^f
$$

$$
\mathbf{r}_f^{k+1}(\bar{\mathbf{u}}, \mathbf{u}^f) \approx \mathbf{r}_f^k + \left(\frac{\partial \mathbf{f}_f^{int}}{\partial \bar{\mathbf{u}}} \bigg|_k \right) \delta\bar{\mathbf{u}} + \left(\frac{\partial \mathbf{f}_f^{int}}{\partial \mathbf{u}^f} \bigg|_k \right) \delta\mathbf{u}^f
$$

Due to the fact that $\bar{\mathbf{f}}_p$ is an unknown entity, let's denote

$$
\delta\bar{\mathbf{f}} \equiv \left(\frac{\partial \bar{\mathbf{f}}_p}{\partial \bar{\mathbf{u}}} \bigg|_k \right) \delta\bar{\mathbf{u}} + \left(\frac{\partial \bar{\mathbf{f}}_p}{\partial \mathbf{u}^f} \bigg|_k \right) \delta\mathbf{u}^f
$$

The tangent stiffness matrix $\mathbf{K}^u$ is defined as

$$
\mathbf{K}^u \equiv \frac{\partial \mathbf{r}^u(\mathbf{u})}{\partial \mathbf{u}} =
\begin{bmatrix}
\mathbf{K}_{pp} = \frac{\partial \mathbf{f}_p^{int}}{\partial \bar{\mathbf{u}}} & \vdots & \mathbf{K}_{pf} = \frac{\partial \mathbf{f}_p^{int}}{\partial \mathbf{u}^f} \\
\cdots\cdots\cdots\cdots & \cdots\vdots\cdots & \cdots\cdots\cdots\cdots \\
\mathbf{K}_{fp} = \frac{\partial \mathbf{f}_f^{int}}{\partial \bar{\mathbf{u}}} & \vdots & \mathbf{K}_{ff} = \frac{\partial \mathbf{f}_f^{int}}{\partial \mathbf{u}^f}
\end{bmatrix}
\tag{3.23}
$$

Finally, equation (3.22) becomes

$$
\begin{cases}
\mathbf{r}_p^{k+1} = \mathbf{r}_p^k + \mathbf{K}_{pp}\delta\bar{\mathbf{u}} + \mathbf{K}_{pf}\delta\mathbf{u}_f + \delta\bar{\mathbf{f}} = \mathbf{0} \\[2mm]
\mathbf{r}_f^{k+1} = \mathbf{r}_f^k + \mathbf{K}_{fp}\delta\bar{\mathbf{u}} + \mathbf{K}_{ff}\delta\mathbf{u}_f = \mathbf{0}
\end{cases}
\Leftrightarrow
\begin{bmatrix}
\mathbf{K}_{pp} & \mathbf{K}_{pf} \\
\mathbf{K}_{fp} & \mathbf{K}_{ff}
\end{bmatrix}
\begin{bmatrix}
\delta\bar{\mathbf{u}} \\
\delta\mathbf{u}_f^k
\end{bmatrix}
= -
\begin{bmatrix}
\mathbf{r}_p(\mathbf{u}^k) + \delta\bar{\mathbf{f}} \\
\mathbf{r}_f(\mathbf{u}^k)
\end{bmatrix}
\tag{3.24}
$$

We can now obtain the value of free displacements' increment $\delta \mathbf{u}_f^k$ and the reaction forces $\delta \bar{\mathbf{f}}$ by solving

$$\mathbf{K}_{ff}\delta\mathbf{u}_f^k = -\mathbf{r}_f(\mathbf{u}^k) - \mathbf{K}_{fp}\delta\bar{\mathbf{u}} \tag{3.25}$$

$$\delta\bar{\mathbf{f}} = -\mathbf{r}_p(\mathbf{u}^k) - \mathbf{K}_{pp}\delta\bar{\mathbf{u}} - \mathbf{K}_{pf}\delta\mathbf{u}_f \tag{3.26}$$

3.2.5 Splitting the elastic energy density and history variable

In this section, we discuss two elements proposed to improve the performance of the phase field model for brittle fracture: *splitting the elastic energy density* $\Psi(\boldsymbol{\epsilon})$ and *introducing the history field* variable $\mathcal{H}$. A tension-compression split of $\Psi(\boldsymbol{\epsilon})$ effectively prevents crack propagation in the regions where the compressive stress dominates. In linear elasticity, $\Psi(\boldsymbol{\epsilon})$ is defined as

$$\Psi(\boldsymbol{\epsilon}) = \frac{1}{2}\boldsymbol{\epsilon} : \mathbb{C} : \boldsymbol{\epsilon} = \frac{1}{2}\lambda\mathrm{tr}^2(\boldsymbol{\epsilon}) + \mu(\boldsymbol{\epsilon} : \boldsymbol{\epsilon}) \quad \text{where } \lambda, \mu \text{ are Lamé parameters}$$

$$\text{Splitting scheme:} \quad \Psi(\boldsymbol{\epsilon}) = \underbrace{\Psi^+(\boldsymbol{\epsilon})}_{Tension} + \underbrace{\Psi^-(\boldsymbol{\epsilon})}_{Compression}$$

The original phase field model of Bourdin *et al.* (2000) uses the no-split strategy of $\Psi(\boldsymbol{\epsilon})$, which resulted in crack growth under compression.

$$\begin{cases} \Psi^+(\boldsymbol{\epsilon}) = \Psi(\boldsymbol{\epsilon}) \\ \Psi^-(\boldsymbol{\epsilon}) = 0 \end{cases} \implies \sigma = g(c)\frac{\partial\Psi}{\partial\boldsymbol{\epsilon}} \tag{3.27}$$

After splitting, the stress degradation function $g(c)$ is only applied to the tension part Ψ^+; thus, the stress tensor is defined as

$$\sigma = g(c)\frac{\partial\Psi^+}{\partial\boldsymbol{\epsilon}} + \frac{\partial\Psi^-}{\partial\boldsymbol{\epsilon}} \tag{3.28}$$

Amor *et al.* (2009) proposed a decomposition strategy based on a deviatoric-volumetric split of strain tensor as following

$$
\begin{cases}
\Psi^+(\boldsymbol{\epsilon}) \equiv \frac{1}{2}K\langle \text{tr}(\boldsymbol{\epsilon})\rangle^2 + \mu(\boldsymbol{\epsilon}^d : \boldsymbol{\epsilon}^d) \\
\Psi^-(\boldsymbol{\epsilon}) \equiv \frac{1}{2}K\langle -\text{tr}(\boldsymbol{\epsilon})\rangle^2
\end{cases}
\quad , \text{ where } \quad
\begin{cases}
\langle a \rangle \equiv \max(a, 0) \\
\boldsymbol{\epsilon}^d \equiv \boldsymbol{\epsilon} - \frac{1}{3}\text{tr}(\boldsymbol{\epsilon})\mathbf{I}
\end{cases}
\tag{3.29}
$$

Regarding the irreversible characteristics of the crack field, Miehe *et al.* (2010a) introduced the *history field* $\mathcal{H} \equiv \max(\Psi^+(\boldsymbol{\epsilon}))$, recording the maximum reference energy of Ψ^+ throughout the loading process. The major benefit of updating $\mathcal{H}$ at each calculation step is that it prevents the cracks from healing when Ψ^+ decreases, thus naturally guaranteeing the irreversibility of the crack. Replacing the term $\mathcal{H}$ in place of Ψ in equation (3.11) of the strong form, equation (3.16, 3.21) of the weak form, we obtain

$$
\frac{c}{l} - l\triangle c = \frac{2(1-c)}{G_c}\mathcal{H} \qquad \text{in } \Omega
\tag{3.30}
$$

$$
\mathbf{r}^c \equiv \int_\Omega \left(lG_c \mathbf{B}_c^T \nabla c + (\frac{G_c}{l} + 2\mathcal{H})\mathbf{N}c - 2\mathcal{H}\mathbf{N}^T \right) dV = \mathbf{0}
\tag{3.31}
$$

$$
\mathbf{K}^c \equiv \frac{\partial \mathbf{r}^c}{\partial \mathbf{c}} = \int_\Omega \left(G_c l(\mathbf{B}^c)^T \mathbf{B}^c + (\frac{G_c}{l} + 2\mathcal{H})\mathbf{N}\mathbf{N}^T \right) dV
\tag{3.32}
$$

3.2.6   Staggered algorithm and energetic stopping criterion

This section discusses the solving strategy for the finite element framework of the phase field model after it has been formed. Theoretically, there are two ways to solve it: using *monolithic solver* to find solutions for the displacement field and crack field simultaneously or *staggered algorithm* to solve them separately. In the former method, only one Newton-Raphson loop is derived from equation (3.17)

$$
\begin{bmatrix} \mathbf{K}^{uu} & \mathbf{K}^{uc} \\ \mathbf{K}^{cu} & \mathbf{K}^{cc} \end{bmatrix} \begin{bmatrix} \delta\mathbf{u} \\ \delta\mathbf{c} \end{bmatrix} = \begin{bmatrix} \mathbf{r}^u \\ \mathbf{r}^c \end{bmatrix}
$$

It seems straightforward and easy to implement, but its robustness is a big issue due to the poor convergence rate. Each successful implementation in this front required additional techniques, such as the line search method by Gerasimov & De Lorenzis (2016) or the penalty method by Msekh *et al.* (2015), among others.

On the other hand, the staggered scheme starts a new load step by finding the displacement from the Newton-Raphson loop in equation (3.25). It then updates the history field, which drives the evolution of the crack field in the next calculation steps. The cracks' value obtained from equation (3.19) impacts the displacement field through the stress degradation function. The staggered loop continues until the stopping criterion, which is based on the free energy, is reached. The free energy functional of the system $E(\mathbf{u}, \mathbf{c})$ consists of the elastic free energy E^u and the crack release energy E^c

$$E(\mathbf{u}, \mathbf{c}) = E^u + E^c, \text{ where } \begin{cases} E^u = \int_\Omega \left[g(c)\Psi_e^+(\boldsymbol{\epsilon}) + \Psi_e^-(\boldsymbol{\epsilon}) \right] dV \\ E^c = \int_\Omega \frac{G_c}{2} \left(\frac{c^2}{l} + l|\nabla c|^2 \right) dV \end{cases} \tag{3.33}$$

The procedure of the staggered algorithm is described as follows:

Algorithm 3.1 Staggered algorithm for brittle fracture

Input: $\mathbf{u}_n, c_n$

Output: $\mathbf{u}_{n+1}, c_{n+1}$

1   **for** $s \leftarrow 1...S$ **do**   // Loop for staggered step

2   COMPUTE DISPLACEMENTS WITH FIXED CRACK

3   Initialize $\mathbf{u}^0_{n+1} = \mathbf{u}_n$;   /* Newton-Raphson loop for $\mathbf{u}$ */

4   Solve $\mathbf{r}^u(\mathbf{u}^k_{n+1}) = \mathbf{0}$;   /* see eq.(3.22 - 3.25) */

5   Update $\mathcal{H}_{n+1} = max(\Psi^+(\mathbf{u}^k_{n+1}), \mathcal{H}_n)$;   /* history variable */

6   COMPUTE CRACK FIELDS WITH FIXED DISPLACEMENTS

7   Initialize $\mathbf{c}^0_{n+1} = \mathbf{c}_n$;   /* Newton-Raphson loop for crack */

8   Solve $\mathbf{r}^c(\mathbf{c}^k_{n+1}) = \mathbf{0}$;   /* see eq.(3.16 - 3.21) */

9   Update crack field $\mathbf{c}_{n+1}$;   /* for degradation function g */

10   COMPUTE ENERGY FUNCTIONAL AND TOLERANCE

11   Calculate E_s and E_{s+1} ;   /* see eq.(3.33) */

12   Calculate $\beta_s = \frac{E_{s+1} - E_s}{E_{s+1}}$;   /* tolerance */

13   **if** $\beta_s \geq TOL$ **then**   // Evaluate tolerance

14   Start a new staggered step $s = s + 1$;   /* with updated $\mathcal{H}$, g */

15   Return to line 2

16   **else**

17   Approve $\mathbf{u}_{n+1}$ and $\mathbf{c}_{n+1}$;   /* Write results */

18   Exit ;   /* then start a new load step */

19   **end if**

20   **end for**

CHAPTER 4

COMPUTATIONAL FRAMEWORK AND IMPLEMENTATION OF PHASE FIELD MODEL FOR FRACTURE IN PLANE STRESS CONDITION

This chapter first introduces a full development in the strain-stress relation under the elastic energy density splitting scheme proposed by Amor *et al.* (2009). It is worth noting that while this explicit form of split strategy is required when integrating it into the finite element framework, its availability is limited in the theoretical aspect. In addition, the simplified strain-stress relation in the plane stress state where all the out-of-plane components of the stress tensor vanish is presented. Next, the computational framework of the phase field model is discussed, opening the door to a tweak that improves its overall flexibility and robustness. At last, two numerical tests are presented to show how the proposed model governs the evolution of the crack.

4.1 Strain-stress's relation in plane stress state

4.1.1 Tensor-based Hooke's law

Amor *et al.* (2009) proposed the splitting strategy in which Ψ is split into volumetric and deviatoric contributions. The stress tensor is then adapted following the elastic energy density split. The noticeable point here is that the stress degradation function $g(c)$ only applies to the volumetric part, which would cause the tension stress.

$$\sigma(\epsilon, c) = g(c)\frac{\partial \Psi^+(\epsilon)}{\partial \epsilon} + \frac{\partial \Psi^-(\epsilon)}{\partial \epsilon}, \quad \text{where} \begin{cases} \Psi^+(\epsilon) \equiv \frac{1}{2}K\langle \text{tr}(\epsilon)\rangle_+^2 + \mu(\epsilon^d : \epsilon^d) \\ \Psi^-(\epsilon) \equiv \frac{1}{2}K\langle \text{tr}(\epsilon)\rangle_-^2 \end{cases}$$

$$\text{and } \langle a\rangle_{\pm} \equiv \frac{1}{2}(a \pm |a|), \quad \epsilon^d \equiv \epsilon - \frac{1}{3}\text{tr}(\epsilon)\mathbf{I}, \quad K \equiv \lambda + \frac{2\mu}{3}$$

$$\Rightarrow \quad \sigma = g(c)\left\{\frac{1}{2}K\left[1 + \text{sign}(tr\epsilon)\right]\langle tr\epsilon\rangle_+ \mathbf{I} + 2\mu\epsilon_d\right\} + \frac{1}{2}K\left[1 - \text{sign}(tr\epsilon)\right]\langle tr\epsilon\rangle_- \mathbf{I}$$

As stress depends on the sign of $tr\epsilon$, it is convenient to split it into two parts: σ^+ and σ^-

• When $tr\epsilon \geq 0$

$$\sigma^+ = g(c)\left\{K\,tr\epsilon\,\mathbf{I} + 2\mu\epsilon_d\right\} \tag{4.1}$$

$$\mathbb{C}^+ = \frac{\partial\sigma^+}{\partial\epsilon} = g\left\{K\,\mathbf{I}\otimes\mathbf{I} + 2\mu\left(\mathbb{I}^s - \frac{1}{3}\mathbf{I}\otimes\mathbf{I}\right)\right\} = g\left(2\mu\mathbb{I}^s + \lambda\mathbf{I}\otimes\mathbf{I}\right) \tag{4.2}$$

• When $tr\epsilon < 0$

$$\sigma^- = g(c)\left\{2\mu\epsilon_d\right\} + K\,tr\epsilon\,\mathbf{I} \tag{4.3}$$

$$\mathbb{C}^- = \frac{\partial\sigma^-}{\partial\epsilon^e} = g\left\{2\mu\left(\mathbb{I}^s - \frac{1}{3}\mathbf{I}\otimes\mathbf{I}\right)\right\} + K\,\mathbf{I}\otimes\mathbf{I} = 2\mu g\mathbb{I}^s + \lambda'\mathbf{I}\otimes\mathbf{I} \tag{4.4}$$

where $\lambda' = \lambda + (1-g)\frac{2\mu}{3}$ and $\mathbb{I}^s = \frac{1}{2}(\delta_{ik}\delta_{jl} + \delta_{il}\delta_{jk})$ – the *symmetric fourth-order unit tensor*.

4.1.2 Simplification for plane stress condition

Within the small strain assumption, i.e. $\epsilon = \nabla^s\mathbf{u} = \frac{1}{2}\left(\nabla\mathbf{u} + \nabla^T\mathbf{u}\right)$, strain tensor ϵ is symmetric and conventionally represented by a six-components vector

$$\begin{bmatrix} \epsilon_{11} & \epsilon_{12} & \epsilon_{13} \\ \epsilon_{12} & \epsilon_{22} & \epsilon_{23} \\ \epsilon_{13} & \epsilon_{23} & \epsilon_{33} \end{bmatrix} \equiv [\epsilon_{11},\ \epsilon_{22},\ ,\epsilon_{33},\ 2\epsilon_{12},\ ,2\epsilon_{23},\ ,2\epsilon_{13}]^T$$

Stress-strain relation in an isotropic elastic solid then becomes

$$\underbrace{\begin{bmatrix} \sigma_{11} \\ \sigma_{22} \\ \sigma_{33} \\ \sigma_{12} \\ \sigma_{23} \\ \sigma_{13} \end{bmatrix}}_{\sigma} = \underbrace{\begin{bmatrix} 2\mu+\lambda & \lambda & \lambda & 0 & 0 & 0 \\ & 2\mu+\lambda & \lambda & 0 & 0 & 0 \\ & & 2\mu+\lambda & 0 & 0 & 0 \\ & & & \mu & 0 & 0 \\ & symmetric & & & \mu & 0 \\ & & & & & \mu \end{bmatrix}}_{\mathbf{C}} \underbrace{\begin{bmatrix} \epsilon_{11} \\ \epsilon_{22} \\ \epsilon_{33} \\ 2\epsilon_{12} \\ 2\epsilon_{23} \\ 2\epsilon_{13} \end{bmatrix}}_{\epsilon}$$

In *plane stress state*, all the stress components related to the third direction are assumed to vanish

$$\sigma_{13} = \sigma_{23} = \sigma_{33} = 0 \tag{4.5}$$

According to the above relationship,

$$\epsilon_{13} = \epsilon_{23} = 0, \qquad \epsilon_{33} = \frac{\lambda}{2\mu + \lambda}(\epsilon_{11} + \epsilon_{22}) = \frac{\nu}{1 - \nu}(\epsilon_{11} + \epsilon_{22})$$

Then we get the compact form for *plane stress state*

$$
\begin{bmatrix} \sigma_{11} \\ \sigma_{22} \\ \sigma_{12} \end{bmatrix}
= \frac{2\mu}{2\mu + \lambda}
\begin{bmatrix}
2(\mu + \lambda) & \lambda & 0 \\
 & 2(\mu + \lambda) & 0 \\
sym & & \frac{2\mu+\lambda}{2}
\end{bmatrix}
\begin{bmatrix} \epsilon_{11} \\ \epsilon_{22} \\ 2\epsilon_{12} \end{bmatrix}
$$

In a similar manner, $\mathbf{C}^+$ and $\mathbf{C}^-$ could be transformed in the matrix format

$$
\underbrace{\begin{bmatrix} \sigma_{11} \\ \sigma_{22} \\ \sigma_{12} \end{bmatrix}}_{\sigma^+}
= \frac{2\mu g}{2\mu + \lambda}
\underbrace{\begin{bmatrix}
2(\mu + \lambda) & \lambda & 0 \\
 & 2(\mu + \lambda) & 0 \\
sym & & \frac{2\mu+\lambda}{2}
\end{bmatrix}}_{\mathbf{C}^+}
\begin{bmatrix} \epsilon_{11} \\ \epsilon_{22} \\ 2\epsilon_{12} \end{bmatrix}
\tag{4.6}
$$

$$
\underbrace{\begin{bmatrix} \sigma_{11} \\ \sigma_{22} \\ \sigma_{12} \end{bmatrix}}_{\sigma^-}
= \frac{2\mu g}{2\mu + \lambda'}
\underbrace{\begin{bmatrix}
2(\mu g + \lambda') & \lambda' & 0 \\
 & 2(\mu g + \lambda') & 0 \\
sym & & \frac{2\mu+\lambda'}{2}
\end{bmatrix}}_{\mathbf{C}^-}
\begin{bmatrix} \epsilon_{11} \\ \epsilon_{22} \\ 2\epsilon_{12} \end{bmatrix}
\tag{4.7}
$$

4.2 Computational framework

4.2.1 Stagggered algorithm: original versus adaptive

Figured (4.1) illustrates how the staggered algorithm works when it is deployed into the computational framework. Although it runs perfectly in a wide range of applications in fracture mechanics, there is a catch: it needs to know the peak of the load-displacement curve where the load ratio is sifted down in order to adapt to the rapidly rising energy potential when the crack occurs. At the breaking point, the energy surface functional increases rapidly, which is the main reason the free energy functional cannot stabilize; thus, the failure occurs when the staggered step reaches its limit, triggering the simulation stoppage.
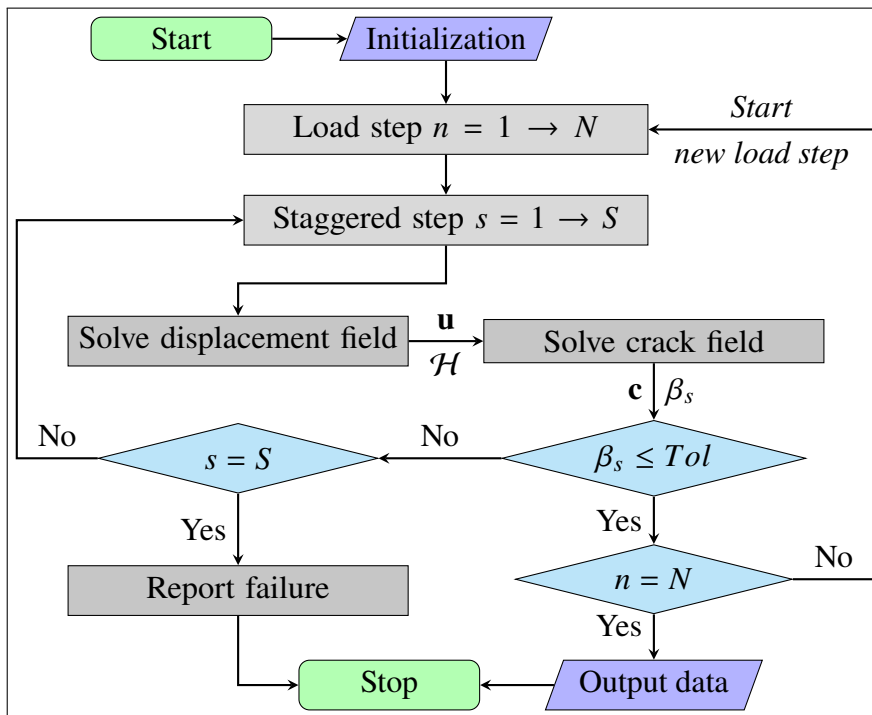

Figure 4.1   Computational framework with original staggered algorithm

It is a common practice to preset the load ratio before running the simulation, forcing it to be a much smaller value before the breaking point, cf. Ambati, Gerasimov & De Lorenzis (2015b);

Molnár & Gravouil (2017). This practice gives leverage for this specific setup, allowing the simulation to go past the breaking point and beyond. Obviously, it is not an optimum and flexible way in reality because the breaking point of a system changes when its geometry or its parameter changes. As the flowchart shows, the only way to obtain information on the system's breaking point is to run a trial simulation and wait until it fails. This step alone can take quite a handful of computational time when the sample is large and consists of a huge set of elements. Even if we are willing to accept to do the trial run, the whole process will become tedious and boring when it includes repetitive simulations, for example, in the parameter analysis. The proposed *adaptive staggered algorithm* offers a resolution for these issues: when the staggered step *s* reaches its maximum value *S*, and the energy potential tolerance β_s is still larger than its threshold value, the *load ratio is automatically adjusted*, and the algorithm will then *repeat the current load step* with the new load ratio. Figure (4.2) describes the flowchart of this adaptive staggered scheme.
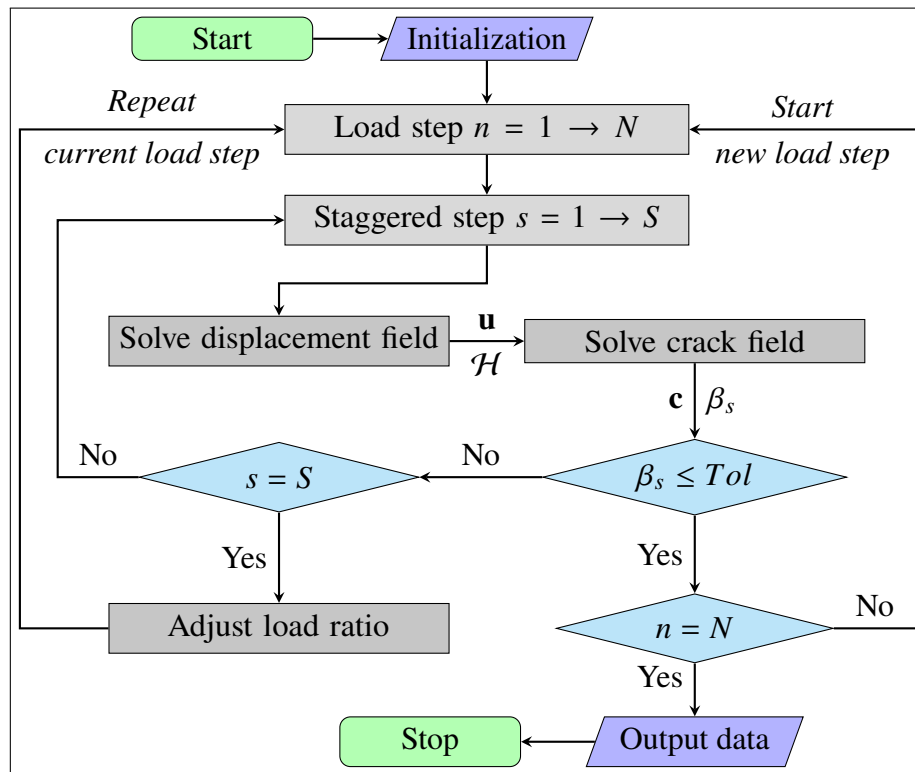

Figure 4.2 Adaptive staggered scheme for plane stress phase-field model

4.2.2 Implementation

This phase field model is implemented entirely in C++. The whole framework includes:

- All the input meshes are created by the freeware GMSH, cf. Geuzaine & Remacle (2009).
- The mesh-reading package is provided by Professor Tan Pham.
- The core computational framework, consisting of two Newton-Raphson algorithms for displacement and crack field; the module for the free energy evaluation, is from the author.
- Library Eigen, cf. Guennebaud, Jacob *et al.* (2010), is utilized to find the solution for the linear algebraic system in the Newton-Raphson loops.
- The post-processing package for the results is from the author.

4.3 Numerical experiments

4.3.1 Setups for single-edge notched test

The single-edge notched test is one of the most popular entry tests for a new phase-field-based fracture model. A solid with a sharp crack in the middle is clamped down at the base. The upper edge is constantly applied a prescribed displacement $\bar{\mathbf{u}}$ in the *vertical direction* $\bar{\mathbf{u}} = (0, 10^{-4}\text{mm})^T$ in the *tension test*; or in the *horizontal direction* $\bar{\mathbf{u}} = (10^{-4}\text{mm}, 0)^T$ in the *shear test*. The *adaptive staggered scheme* will automatically adjust the magnitude of $\bar{\mathbf{u}}$ when the crack initiates to avoid convergence failure of the staggered algorithm. The simulation continues until the sample is totally broken. Figure (4.4) illustrates the detailed setups for the two tests.

The objective of the *tension test* is twofold. The first one is to *verify whether the crack will grow horizontally* until the sample is totally broken, a fact that is widely accepted and validated in both plane strain and three-dimensional configuration, cf. Miehe *et al.* (2010a,b); Ambati *et al.* (2015b); Molnár & Gravouil (2017). The second one is to *conduct the parameter analysis* for two essential parameters of the phase field model for fracture: *the length scale l* and *the ratio of the length scale over the mesh size l/h*.
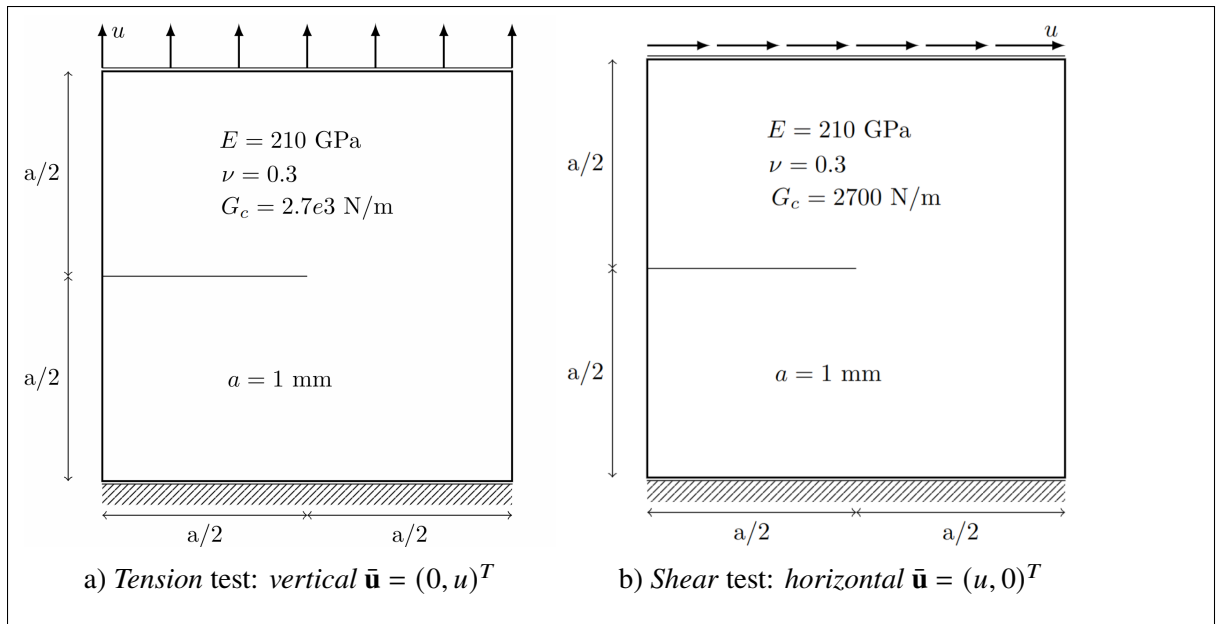
Figure 4.3   The single-edge notched test in two different loading schemes

4.3.2   Results and discussions for tension test

In this test, the order for running the simulation is as follows:

- First, three runs on a *uniform mesh* with three different length scales are performed to see how the framework processes the crack's evolution.

- Second, eight simulations are employed on the same non-uniform *coarse mesh* for the parameter analysis.

- Third, six simulations are carried out on the finer *medium mesh* to solidify what has been found in the second round.

Table (4.1) summarizes all the simulations performed on three different meshes. The terms *coarse* and *medium* are used for the non-uniform meshes as an alias to differentiate them. The key difference in those meshes is the *mesh size*, defined as the longest edge of an element, within the *area of interest*, where elements are concentrated the most, as we can see in Figure (4.4).

Table 4.1   Summary of all the simulations in the tension test.

Order	Mesh characteristics			Length scale**	Ratio
	Alias	*Total elements*	*Mesh size**		
1	Uniform	10000	$h = 0.01$	$l = 0.1$	$r = 10$
2	Uniform	10000	$h = 0.01$	$l = 0.05$	$r = 5$
3	Uniform	10000	$h = 0.01$	$l = 0.03$	$r = 3$
4	Coarse	4560	$h \approx 4 \times 10^{-3}$	$l_1 = 0.015$	
5	Coarse	4560	$h \approx 4 \times 10^{-3}$	$l_2 = 0.03$	
6	Coarse	4560	$h \approx 4 \times 10^{-3}$	$l_3 = 0.05$	
7	Coarse	4560	$h \approx 4 \times 10^{-3}$	$l_4 = 0.075$	
8	Coarse	4560	$h \approx 4 \times 10^{-3}$		$r_1 = 3$
9	Coarse	4560	$h \approx 4 \times 10^{-3}$		$r_2 = 5$
10	Coarse	4560	$h \approx 4 \times 10^{-3}$		$r_3 = 10$
11	Coarse	4560	$h \approx 4 \times 10^{-3}$		$r_4 = 20$
12	Medium	8951	$h \approx 2.5 \times 10^{-3}$	$l_1 = 0.015$	
13	Medium	8951	$h \approx 2.5 \times 10^{-3}$	$l_2 = 0.03$	
14	Medium	8951	$h \approx 2.5 \times 10^{-3}$	$l_3 = 0.05$	
15	Medium	8951	$h \approx 2.5 \times 10^{-3}$		$r_2 = 5$
16	Medium	8951	$h \approx 2.5 \times 10^{-3}$		$r_3 = 10$
17	Medium	8951	$h \approx 2.5 \times 10^{-3}$		$r_4 = 20$

* Mesh size in the interest area for the non-uniform mesh in millimeters [mm]

** Fixed characteristics length scale in millimeters [mm]

The numerical experiment begins with a *uniform mesh* containing 10000 quadrilateral elements (Q4). Whereas it is quite a large number of elements, its unique mesh size, $h = 0.01$ mm, is still considered a "coarse" size in the phase-field community. A set of three fixed values of length scale $l = (0.03,\ 0.05,\ 0.1)$mm is applied to this mesh to study the crack's evolution as well as

the effect on the localization of the crack. Figure (4.5) shows two things: first, cracks grow horizontally; second, the bandwidth of the damaged regime shrinks when the length scale is reduced from $l = 0.1$ to 0.03mm, implying that the shorter l becomes, the narrower the range of the crack field will be. Coincidentally, this fact is in agreement with the $\Gamma-$convergence theory of Braides (1998): when $l \to 0$, the smeared crack reverses to its sharp state. In terms of brittle behavior, when we look at the difference between prescribed u at the time the solid is totally broken and at the time when the crack starts:

$$\Delta u(l = 0.03) = 8.9 \times 10^{-5} < \Delta u(l = 0.05) = 9 \times 10^{-5} < \Delta u(l = 0.1) = 2.92 \times 10^{-4}$$

That means the sample applied with a shorter length scale behaves more brittle than one with a longer length scale because it reaches the total failure faster.
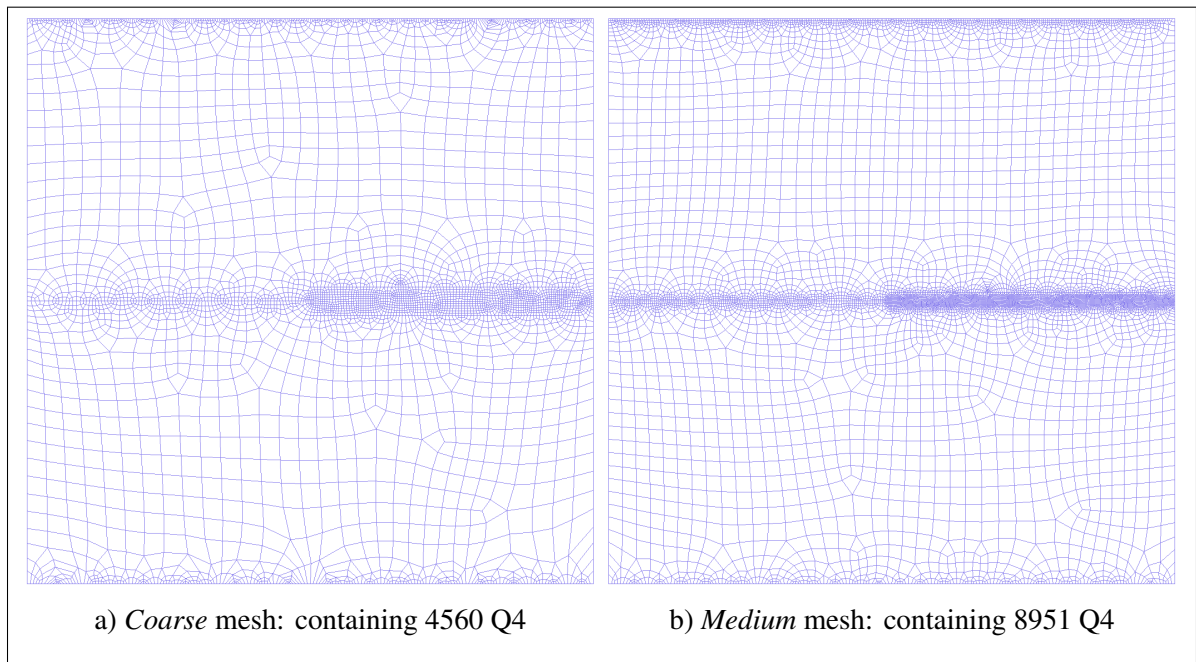

a) *Coarse* mesh: containing 4560 Q4   b) *Medium* mesh: containing 8951 Q4

Figure 4.4   Two non-uniform meshes used in the tension test.

a) $l = 0.1$mm : crack starts
$u = 0.003$ mm

b) $l = 0.1$mm : propagates
$u = 0.00315$mm

c) $l = 0.1$mm : totally broken
$u = 3.292 \times 10^{-3}$ mm

d) $l = 0.05$mm : crack starts
$u = 0.0031$ mm

e) $l = 0.05$mm : propagates
$u = 0.00315$ mm

f) $l = 0.05$mm : totally broken
$u = 3.19 \times 10^{-3}$mm

g) $l = 0.03$mm : crack starts
$u = 0.00312$

h) $l = 0.03$mm : propagates
$u = 0.0315$ mm

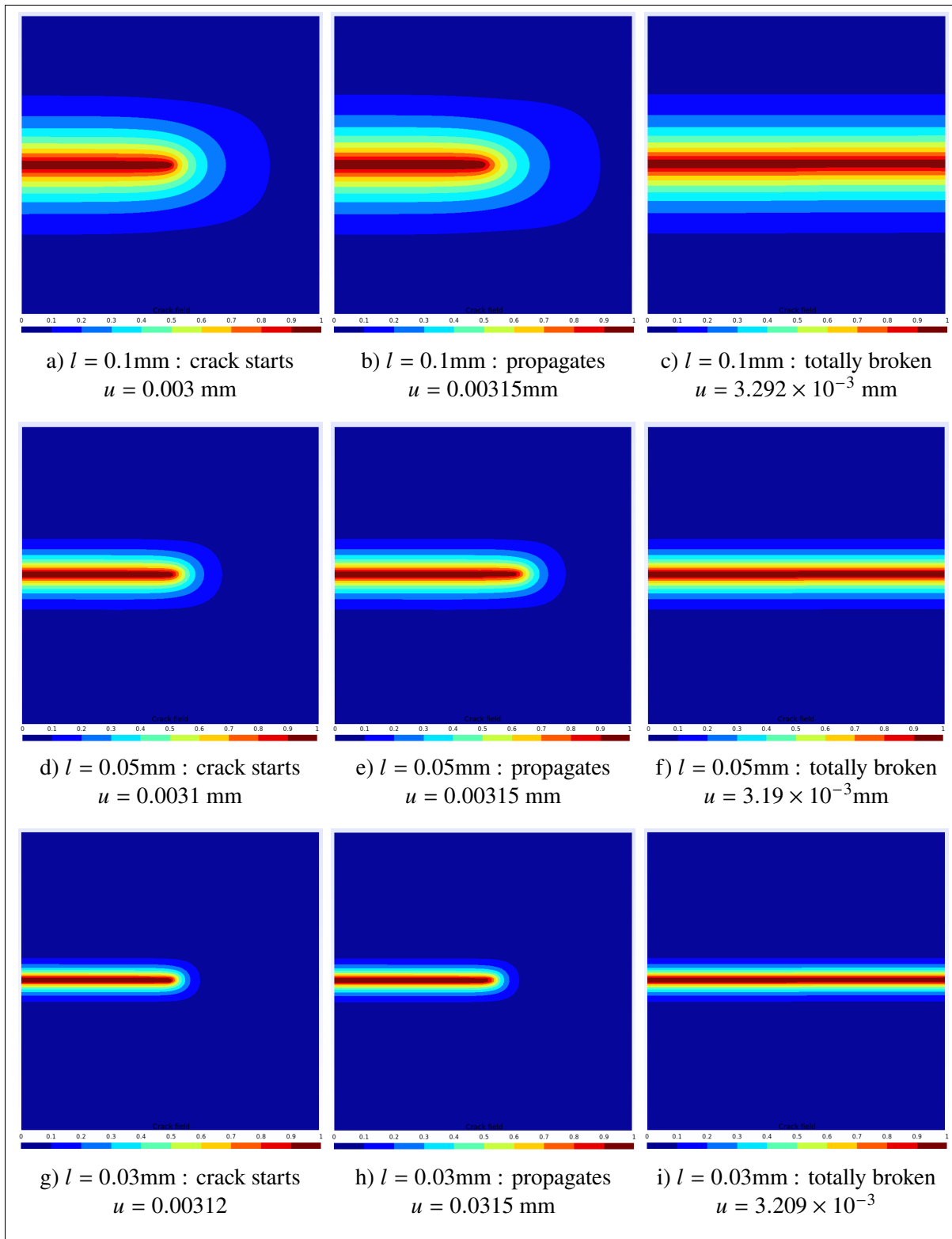i) $l = 0.03$mm : totally broken
$u = 3.209 \times 10^{-3}$

Figure 4.5   The crack's evolution in the uniform mesh containing 10000 Q4.

Turning now to the parameter analysis, two parameters will be studied in detail to determine how they regulate the crack growth in this phase field model:

- The first parameter is the characteristics length scale l: a fixed value of length scale will be applied to all elements of a mesh. In the simulation of order $4 - 7$ in Table (4.1), four different fixed length scales are applied on the *coarse mesh* separately. Similarly, in order 12 – 14 simulations, three various values of length scale are applied on the *medium mesh*.

- The second parameter is the ratio r between the length scale and the mesh size, i.e., $r = l/h$: a fixed value of ratio r requires the calculation of the length scale at each element because the mesh size h varies in the non-uniform mesh. Each simulation from the order of $8 - 11$ uses a different fixed ratio on the *coarse mesh*, and the simulation from the order of $15 - 17$ uses either the ratio of $r = 5$, $r = 10$, or $r = 20$ on the *medium mesh*.

What can be clearly seen in Figure (4.6) is the deflection of the crack's trajectory from the horizontal line at the fixed ratio $r_1 = 3$, $r_2 = 5$ and $r_3 = 10$, which is not expected given various references from the literature, cf. Molnár & Gravouil (2017); Ambati *et al.* (2015b); Miehe *et al.* (2010b). As a result, the load-displacement curves corresponding to these fixed ratios become outliners, among others in the Figure (4.7). To be more specific, the sooner the deflection happens, the longer it takes to reach the dramatic drop in the load-displacement curve. The fact that the same observation can be found in the simulations on the finer mesh (*medium mesh*), see Figure (4.8 – 4.9), implies that even if the fixed ratio satisfies the least requirement from Miehe *et al.* (2010a), i.e., $r = l/h > 2$, it does not necessarily guarantee the correct trajectory of the crack.

a) $r_1 = 3$
Deflect at halfway

b) $r_2 = 5$
Deflect at halfway

c) $r_3 = 10$
Deflect at the end

d) $r_4 = 20$
No deflection

e) $l_1 = 0.015$mm

f) $l_2 = 0.03$mm
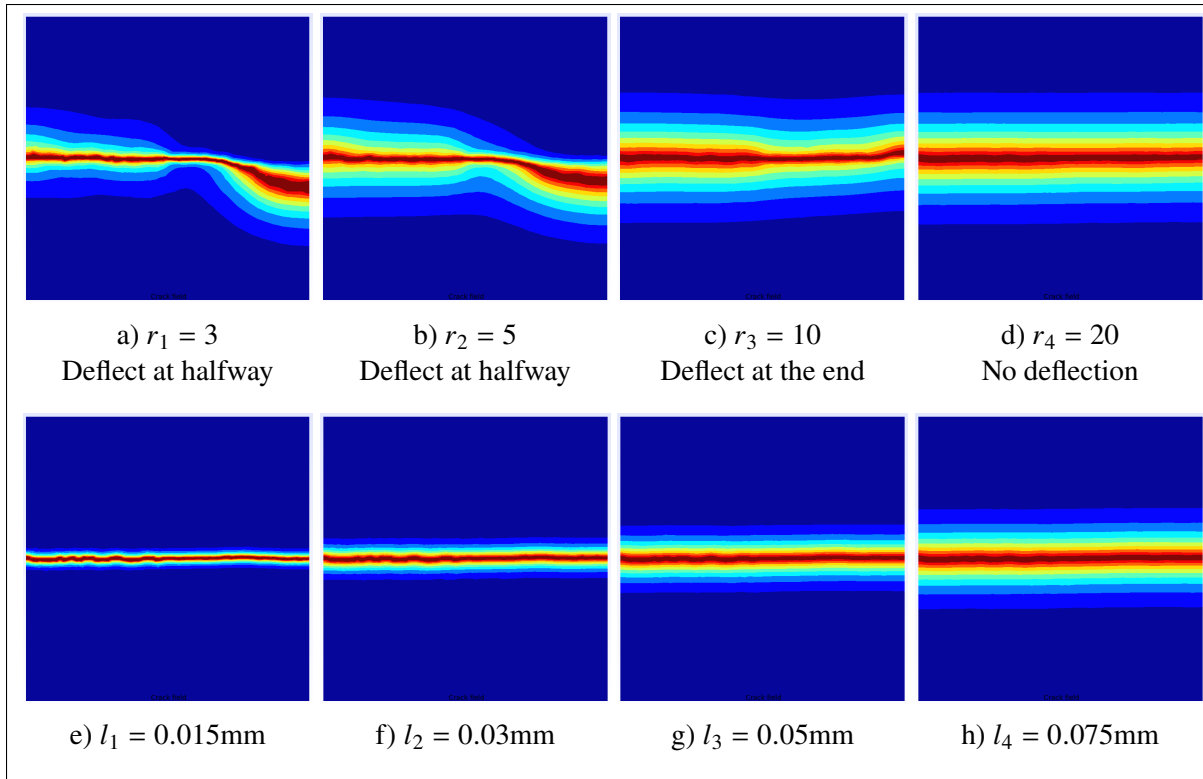
g) $l_3 = 0.05$mm

h) $l_4 = 0.075$mm

Figure 4.6   The crack path at the end of load cycle in the *coarse mesh*: ratio-controlled length scale in the first row and fixed length scale in the second row
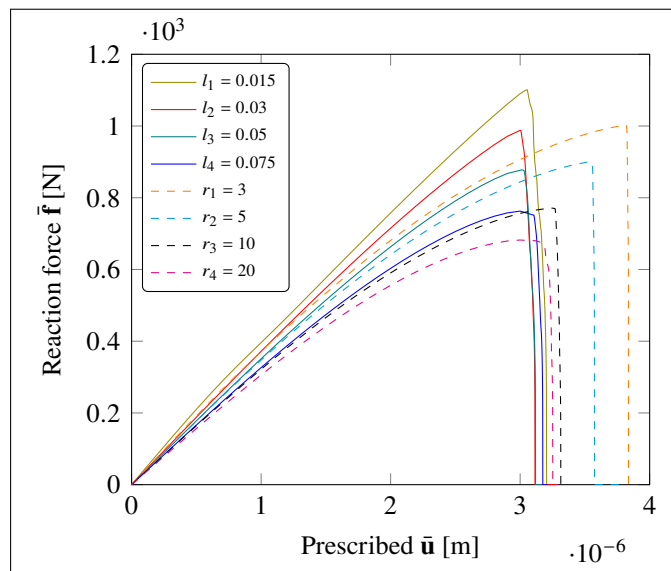

Figure 4.7   Load-displacement curve of the *coarse mesh* – fixed versus ratio-controlled length scale
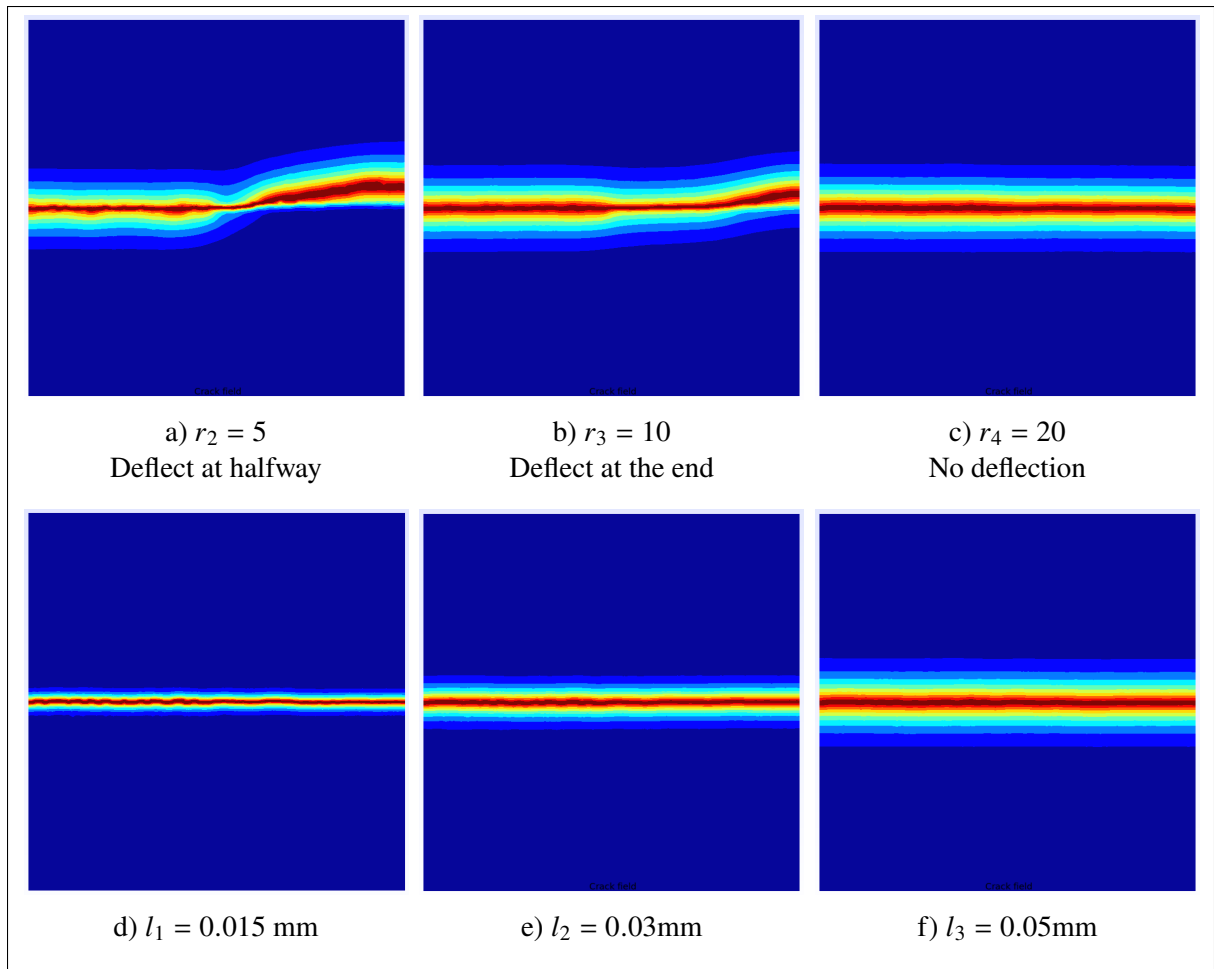
Figure 4.8   The crack path at the end of load cycle in the *medium mesh*: ratio-controlled
length scale in the first row and fixed length scale in the second row

In conclusion, after performing a series of simulations on three different meshes, these are
noticeable observations:

- The crack propagates horizontally in most cases, as expected.
- The *length scale* stands out as a more reliable parameter in this phase field model for fracture.
- All the simulations in the tension test run smoothly without failure and, especially, do not need the system's breaking point beforehand to proceed.
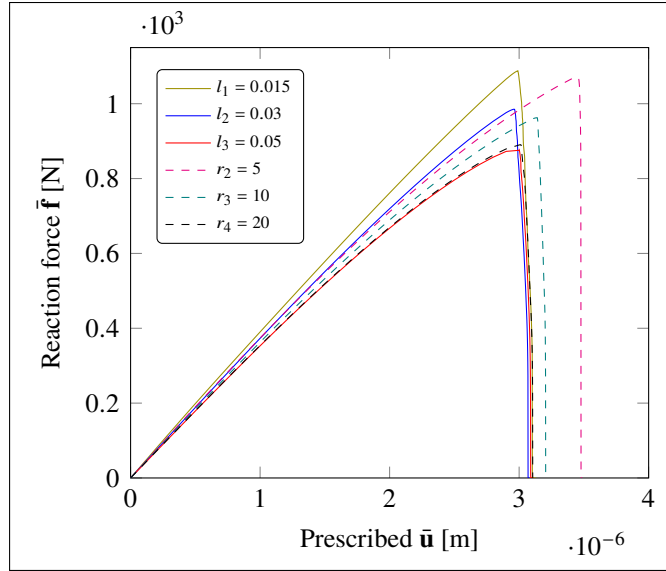
Figure 4.9   Load-displacement curve of the *medium mesh* – fixed versus ratio-controlled length scale

4.3.3   Results and discussions for shear test

While the tension test has already verified the model's ability to propagate the crack automatically, the purpose of the shear test is to double-check whether the splitting strategy of the elastic energy density works well in this model. With the loading scheme as described in Figure (4.4), the crack is expected to grow downward from the center toward the right-bottom corner of the sample, cf. Miehe *et al.* (2010b); Ambati *et al.* (2015b); Molnár & Gravouil (2017). With regard to prescribed displacement, $\bar{\mathbf{u}} = (10^{-4}\text{mm}, 0)^T$ from the start to the breaking point of the load-displacement curve, then it is set at $(10^{-5}\text{mm}, 0)^T$ until the sample is totally broken.
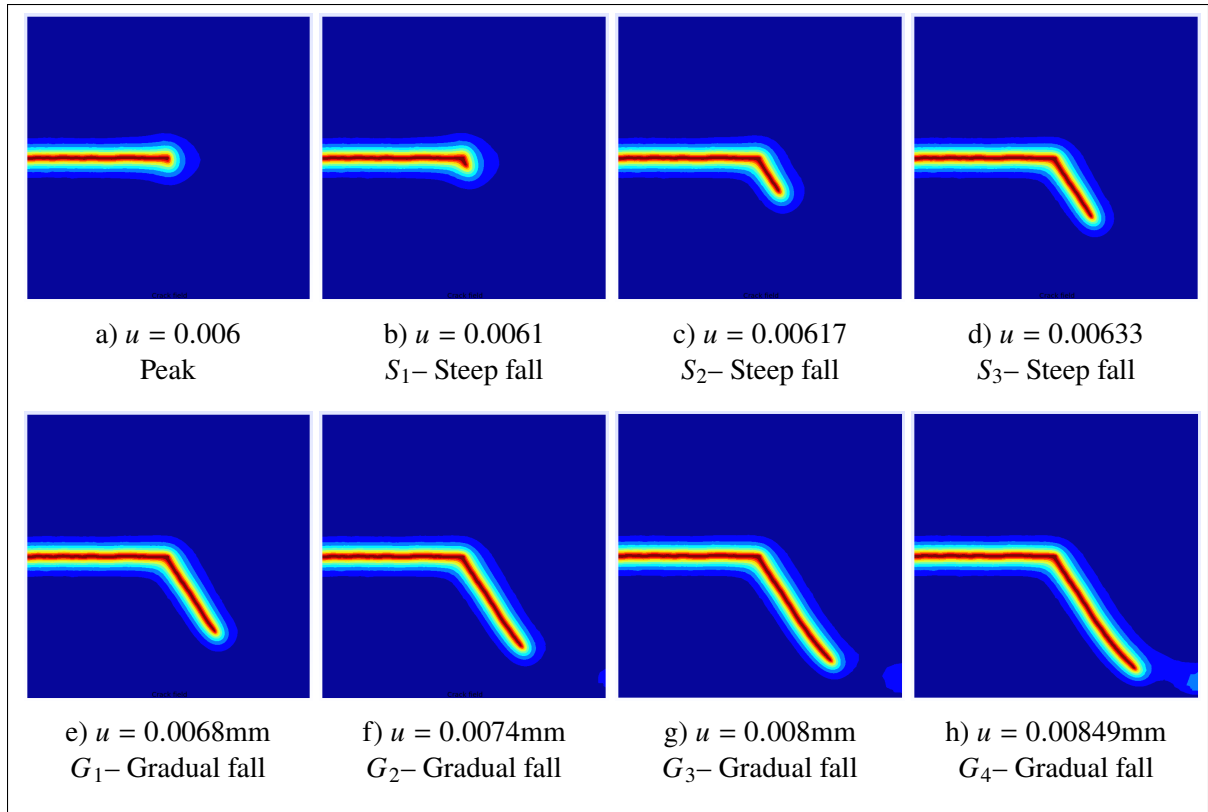
Figure 4.10   The evolution of crack in the shear test of the sample consisting of 10406 Q4 elements: crack trajectories correspond with eight marks on Figure (4.11)

What stands out in Figure (4.10) is the steady growth downward of the crack field, implying the strain decomposition in the splitting strategy worked wonderfully in the framework. As a result, it prevents the crack from propagating into the upper part of the sample, where the compression strain dominates under this loading scheme. Moreover, Figure (4.11) shows that the drop of the load-displacement curve can be split into two stages:

- The first stage begins from the peak, where the crack starts to grow, to the point marked as S_3 in the curve. The crack propagates quickly, nearly half of its trajectory gained in this stage, which is why it is called *steep fall*.

- The second stage starts from S_3: the crack gradually grows towards the left bottom of the sample until it reaches the totally broken point. That is why this stage is called *gradual fall*.
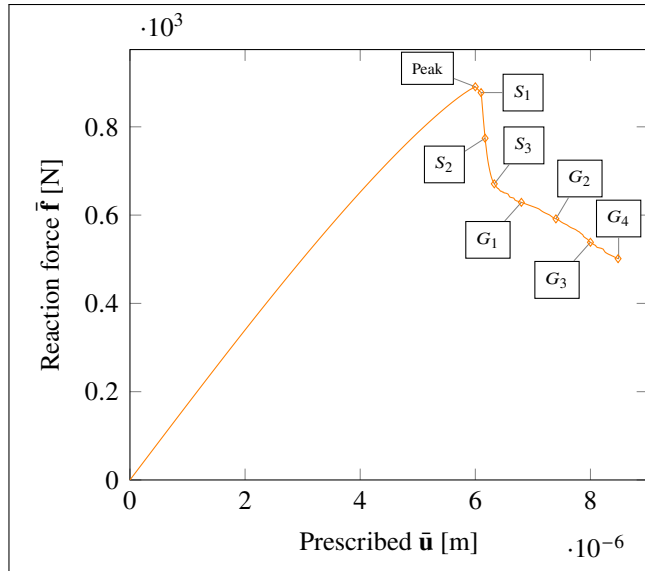
Figure 4.11   Load-displacement curve of the
shear test on the sample containing 10406 Q4
elements, length scale $l = 0.03$ mm

4.3.4   Convergence rate

The staggered algorithm consists of three calculation blocks: two Newton-Raphson loops to solve displacement and crack; and one block to evaluate the free energy functional. As the two Newton-Raphson iterations inside the staggered algorithm converge quickly, with only 1-2 steps in each loop, the stability of free energy is the key to the convergence of the staggered loop.

As the number of staggered steps per load step varies throughout the load-displacement curve of the simulation, let us break down the curve into stages where the number of staggered steps can be differentiated from each other. For this purpose, the load-displacement curve recorded from the tension test, summarized in Table (4.1), can be divided into three stages:

- The first stage starts from the beginning to the area near the breaking point, which is called *Pre-peak*. In this framework, when applying *adaptive staggered scheme*, the *Pre-peak* is determined as the first load steps after the algorithm decreases the load ratio due to the failure in the current load step and restarts it.

- The second stage is from the *Pre-peak* to the *Peak*, where the crack starts to grows. It usually takes 5 to 10 load steps for the curve to peak.
- The third stage begins after the breaking point and is called *Post-peak*.

Table (4.2) shows that the number of staggered steps per load step increases when the curve reaches its peak, underscores the instability of the free energy when the solid reaches its breaking point. A point worth noting here is that when the curve enters the *Pre-peak* zone, its load ratio has already been reduced by at least one-tenth of the value from the start, which reminds us how volatile the free energy becomes at this zone. This is where the *adaptive staggered scheme* shows its flexibility: it only needs one load step with a maximum staggered step, reduces the load ratio, and then starts the load steps over with a higher possibility of stabilizing the solid's free energy. Moreover, this algorithm would save quite an amount of computing time in comparison to the original version in both scenarios: either the pre-defined breaking point is before or after the actual peak. In the first case, it would take much more computing time than usual: a smaller load ratio couples with more staggered steps when it is near the peak. The second case is worse: the free energy is unlikely to converge, the algorithm fails, and we must start from scratch.

Table 4.2   Breakdown of the number of staggered steps
per load step in different stages of the tension test

Sample	Number of staggered steps per load step		
	Start to Pre-peak	*Pre-peak*	*Post-peak*
Coarse	$3 - 8$	$10 - 12$	$10 - 20$
Medium	$3 - 8$	$10 - 12$	$10 - 30$
Uniform	$3 - 10$	$10 - 20$	$10 - 20$

As discussed on the result of the shear test, Figure (4.11) shows that the load-displacement behaves differently after the breaking point, adding the two stages of *Steep fall* and *Gradual fall* instead of *Post-peak* in the tension test. The report in Table (4.3) reveals that while the algorithm

took more staggered steps, i.e., computational time, to converge in the *steep fall* stage, the crack grew fastest at the same time, as illustrated in Figure (4.10).

Table 4.3   Breakdown of the number of staggered steps
per load step in different stages of the shear test

Sample	Number of staggered steps per load step			
	Start to Pre-peak	*Pre-peak*	*Steep fall*	*Gradual fall*
Mesh containing 10406 quads	3 − 7	10	10 − 20	4 − 6

To conclude, the advantages of the proposed finite element model are:

- The fact that all the simulations in the tension test and shear test run smoothly despite the dramatic drop in the load-displacement curve of brittle fracture confirms the robustness of the computational framework.

- The *adaptive staggered scheme* offers the flexibility that the original algorithm lacks when the system reaches its breaking point.

- Energy-based stopping criterion used in the staggered algorithm makes more physical sense than the crack field-based criterion, cf. Bourdin *et al.* (2000).

CONCLUSION AND RECOMMENDATIONS

This study was undertaken to develop a phase-field-based fracture model in the plane stress state, implement it in C++, and conduct two popular numerical experiments to compare the evolution of the crack with the existing models' results. The computational framework includes two new developments:

- To construct the material's behavior in *plane stress* state while incorporating a splitting scheme of elastic energy to prevent cracking under compression. It leads to a nonlinear system of displacement that needs a Newton-Raphson scheme to solve.

- To propose an *adaptive* scheme to make the framework more flexible when it reaches the breaking point, thus improving its robustness and reducing computational time.

The developed model performs smoothly under two different loading schemes, delivering the fracture mechanism, such as crack opening and crack propagation, in both testing cases. Also, this research extends our knowledge of the phase-field-based fracture model, such as the importance of length scale and the pitfall involving the ratio between length scale and mesh size.

This work will serve as a base for future studies because its energetic concept opens to couple with other energy-based phenomena such as temperature or plasticity by adding their corresponding energy (thermal or plastic) to the free energy functional, then modifying the development.

Finally, a number of important limitations need to be considered. First, this implementation uses a serial solver, which proves inadequate when the mesh size is large. It leads to the recommendation for future work: to use a powerful parallel solver to solve the linear system equations. Secondly, mesh samples used in tension and shear tests are well-refined in the area where cracks could occur to better represent its geometry. Choosing where to refine the mesh might be challenging in reality, especially in complex geometries. Assessing a simple adaptive meshing scheme where only elements' crack fields reached a certain value to be refined would be interesting.

STRESS-STRAIN RELATION AND ELASTIC ENERGY DENSITY IN PLANE STRAIN CONDITION

1. Simplification for plane strain condition

In *plane strain state*, all the strain components related to the third direction cease to exist, i.e.

$$\epsilon_{13} = \epsilon_{23} = \epsilon_{33} = 0$$

$$
\begin{bmatrix} \sigma_{11} \\ \sigma_{22} \\ \sigma_{33} \\ \sigma_{12} \\ \sigma_{23} \\ \sigma_{13} \end{bmatrix}
=
\begin{bmatrix}
2\mu + \lambda & \lambda & \lambda & 0 & 0 & 0 \\
 & 2\mu + \lambda & \lambda & 0 & 0 & 0 \\
 & & 2\mu + \lambda & 0 & 0 & 0 \\
 & & & \mu & 0 & 0 \\
 & symmetric & & & \mu & 0 \\
 & & & & & \mu
\end{bmatrix}
\begin{bmatrix} \epsilon_{11} \\ \epsilon_{22} \\ 0 \\ 2\epsilon_{12} \\ 0 \\ 0 \end{bmatrix}
$$

$$
\Rightarrow
\begin{cases}
\sigma_{13} = \sigma_{23} = 0 \\
\sigma_{33} = \frac{\lambda}{2(\mu+\lambda)}(\sigma_{11} + \sigma_{22}) = \nu(\sigma_{11} + \sigma_{22})
\end{cases}
$$

$$
\xrightarrow{Simplified}
\begin{bmatrix} \sigma_{11} \\ \sigma_{22} \\ \sigma_{12} \end{bmatrix}
=
\begin{bmatrix}
2\mu + \lambda & \lambda & 0 \\
 & 2\mu + \lambda & 0 \\
sym & & \mu
\end{bmatrix}
\begin{bmatrix} \epsilon_{11} \\ \epsilon_{22} \\ 2\epsilon_{12} \end{bmatrix}
$$

Decomposing stress tensor

$$\begin{bmatrix} \sigma_{11} \\ \sigma_{22} \\ \sigma_{12} \end{bmatrix} = g \begin{bmatrix} 2\mu + \lambda & \lambda & 0 \\ & 2\mu + \lambda & 0 \\ sym & & \mu \end{bmatrix} \begin{bmatrix} \epsilon_{11} \\ \epsilon_{22} \\ 2\epsilon_{12} \end{bmatrix} \tag{A I-1}$$

$$\underbrace{\sigma^+}_{} \qquad \underbrace{\mathbf{C}^+}_{}$$

$$\begin{bmatrix} \sigma_{11} \\ \sigma_{22} \\ \sigma_{12} \end{bmatrix} = \begin{bmatrix} 2\mu g + \lambda' & \lambda' & 0 \\ & 2\mu g + \lambda' & 0 \\ sym & & \mu g \end{bmatrix} \begin{bmatrix} \epsilon_{11} \\ \epsilon_{22} \\ 2\epsilon_{12} \end{bmatrix} \tag{A I-2}$$

$$\underbrace{\sigma^-}_{} \qquad \underbrace{\mathbf{C}^-}_{}$$

2.   Evaluation of elastic energy density Ψ

$$\Psi(\epsilon) = \frac{1}{2}\epsilon : \mathbf{C} : \epsilon = \frac{1}{2}\lambda \mathrm{tr}^2(\epsilon) + \mu(\epsilon : \epsilon)$$

where Lamé parameters $\lambda = \dfrac{E\nu}{(1+\nu)(1-2\nu)}, \qquad \mu \equiv G = \dfrac{E}{2(1+\nu)}$

Decomposing Ψ into volumetric and deviatoric contributions blocks the crack spread under compression condition.

$$\Psi(\epsilon) = \Psi^+ + \Psi^-, \text{ where } \begin{cases} \Psi^+(\epsilon) \equiv \frac{1}{2}K\langle \mathrm{tr}(\epsilon)\rangle_+^2 + \mu(\epsilon^d : \epsilon^d) \\ \Psi^-(\epsilon) \equiv \frac{1}{2}K\langle \mathrm{tr}(\epsilon)\rangle_-^2 \end{cases}$$

$$\langle a\rangle_\pm \equiv \frac{1}{2}(a \pm |a|), \quad \epsilon^d \equiv \epsilon - \frac{1}{3}\mathrm{tr}(\epsilon)\mathbf{I}, \quad K \equiv \lambda + \frac{2\mu}{3}$$

- In *plane stress* condition, strain tensor ϵ and its deviatoric tensor ϵ^d read

$$\epsilon \equiv \begin{bmatrix} \epsilon_{11} \\ \epsilon_{22} \\ \epsilon_{12} \end{bmatrix}, \quad \epsilon_{33} = \frac{\nu}{\nu - 1}(\epsilon_{11} + \epsilon_{22})$$

$$\epsilon^d \equiv \begin{bmatrix} \epsilon_{11} - \frac{1}{3}\mathrm{tr}(\epsilon) \\ \epsilon_{22} - \frac{1}{3}\mathrm{tr}(\epsilon) \\ \epsilon_{12} \end{bmatrix}, \quad \epsilon_{33}^d = \frac{\nu + 1}{3(\nu - 1)}(\epsilon_{11} + \epsilon_{22})$$

$$\implies \begin{cases} \mathrm{tr}(\epsilon) \equiv \epsilon_{11} + \epsilon_{22} + \epsilon_{33} = \frac{2\nu - 1}{\nu - 1}(\epsilon_{11} + \epsilon_{22}) \\ \epsilon^d : \epsilon^d = [\epsilon_{11} - \frac{1}{3}\mathrm{tr}(\epsilon)]^2 + [\epsilon_{22} - \frac{1}{3}\mathrm{tr}(\epsilon)]^2 + 2\epsilon_{12}^2 + (\epsilon_{33}^d)^2 \end{cases}$$

- In *plane strain* condition,

$$\epsilon \equiv \begin{bmatrix} \epsilon_{11} \\ \epsilon_{22} \\ \epsilon_{12} \end{bmatrix}, \quad \epsilon^d \equiv \begin{bmatrix} \epsilon_{11} - \frac{1}{3}\mathrm{tr}(\epsilon) \\ \epsilon_{22} - \frac{1}{3}\mathrm{tr}(\epsilon) \\ \epsilon_{12} \end{bmatrix}$$

$$\implies \begin{cases} \mathrm{tr}(\epsilon) \equiv \epsilon_{11} + \epsilon_{22} + \epsilon_{33} = \epsilon_{11} + \epsilon_{22} \\ \epsilon^d : \epsilon^d = [\epsilon_{11} - \frac{1}{3}\mathrm{tr}(\epsilon)]^2 + [\epsilon_{22} - \frac{1}{3}\mathrm{tr}(\epsilon)]^2 + 2\epsilon_{12}^2 \end{cases}$$

- Decomposing the elastic energy density $\Psi(\epsilon) = \Psi^+ + \Psi^-$

$$\text{When } \mathrm{tr}(\epsilon) \geq 0 \implies \begin{cases} \Psi^+ = \frac{1}{2}K\mathrm{tr}(\epsilon)^2 + \mu(\epsilon^d : \epsilon^d) \\ \Psi^- = 0 \end{cases}$$

$$\text{When } \mathrm{tr}(\epsilon) < 0 \implies \begin{cases} \Psi^+ = \mu(\epsilon^d : \epsilon^d) \\ \Psi^- = \frac{1}{2}K\mathrm{tr}(\epsilon)^2 \end{cases}$$

APPENDIX II

THE FORM OF THE DEGRADATION FUNCTION

The degradation function $g(c)$ plays a crucial role in the phase field model, connecting mechanical deformation in the equilibrium equation and the crack field in the regularized counterpart. The chosen function has to satisfy the following criteria mathematically:

- Guarantee the full response of internal force in case of intact ($c = 0$) and vice versa, i.e.

$$g(0) = 1, \text{ and } \quad g(1) = 0$$

- Must be a monotonically decreasing function

$$g'(c) \equiv \frac{\partial g}{\partial c} < 0$$

- Prevent the crack grow orthogonally

$$g'(1) = 0$$

Some common degradation functions are presented in Table(II-1). The original quadratic form introduced by Bourdin *et al.* (2000) is widely used in mechanical models, especially for brittle fractures.

Table-A II-1   Phase-field models with different forms of
degradation function

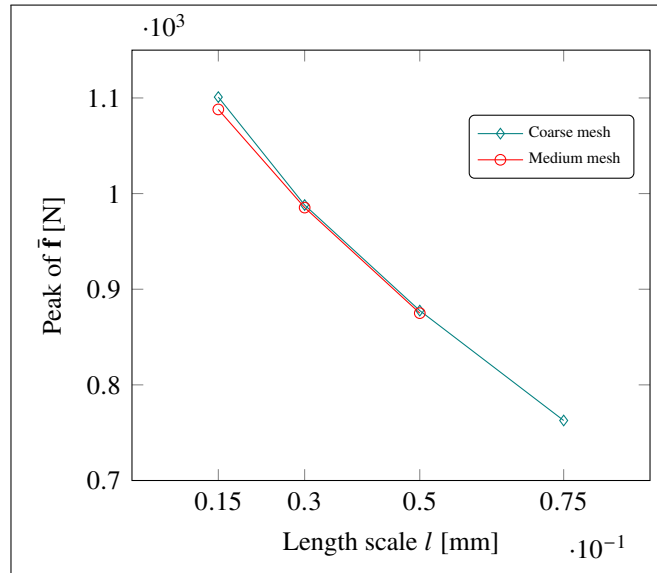| Degradation form $g(c)$	Authors (Year)	Remarks
$(1 - c)^2$	Bourdin *et al.* (2000)	Original quadratic form
$3(1 - c)^2 - 2(1 - c)^3$	Karma, Kessler & Levine (2001)	For dynamic fracture
$4(1 - c)^3 - 3(1 - c)^4$	Kuhn, Schlüter & Müller (2015)	Focus on crack nucleation

ADDITIONAL FIGURES

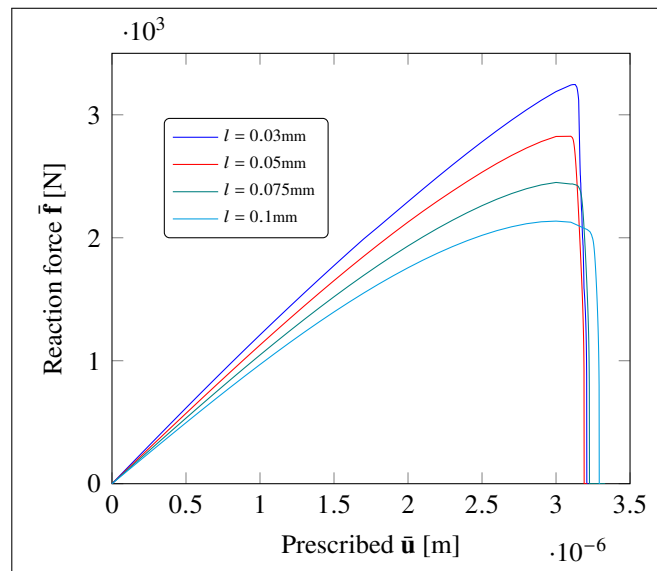Figure-A III-1   Peak of load-displacement curve versus length
scale

Figure-A III-2   Load-displacement curve of mesh containing
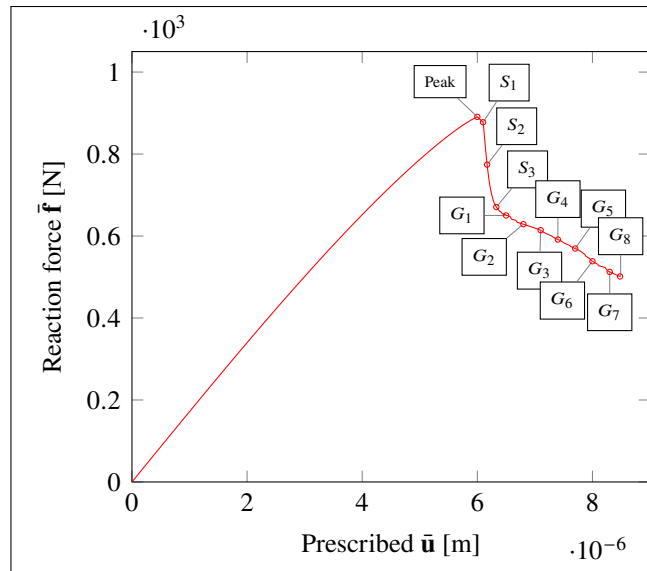10000 Q4 elements

Figure-A III-3   Load-displacement curve in the shear test of
sample containing 10406 Q4 elements – Length scale is set at
$l = 0.03$mm

| a) $u = 0.006$ | b) $u = 0.0061$ | c) $u = 0.00617$ | d) $u = 0.00633$ | e) $u = 0.0065$ | f) $u = 0.0068$ |
| Peak | S_1– steep | S_2– steep | S_3– steep | G_1– gradual | G_2– gradual |

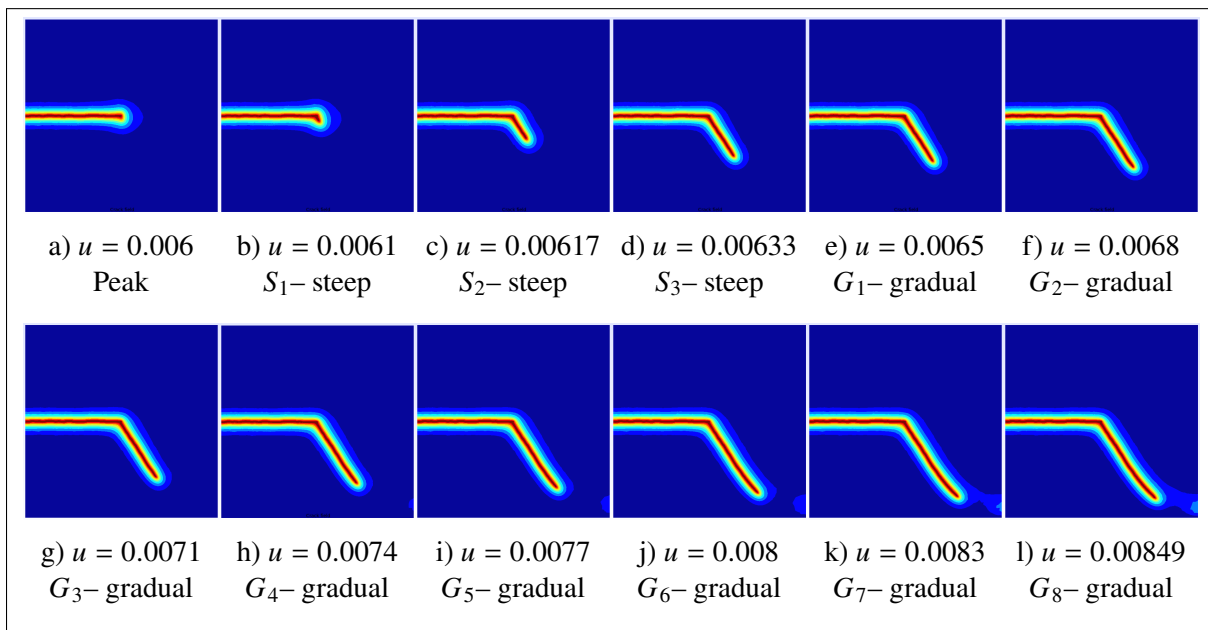| g) $u = 0.0071$ | h) $u = 0.0074$ | i) $u = 0.0077$ | j) $u = 0.008$ | k) $u = 0.0083$ | l) $u = 0.00849$ |
| G_3– gradual | G_4– gradual | G_5– gradual | G_6– gradual | G_7– gradual | G_8– gradual |

Figure-A III-4   The evolution of crack in the shear test of the sample consisting of 10406
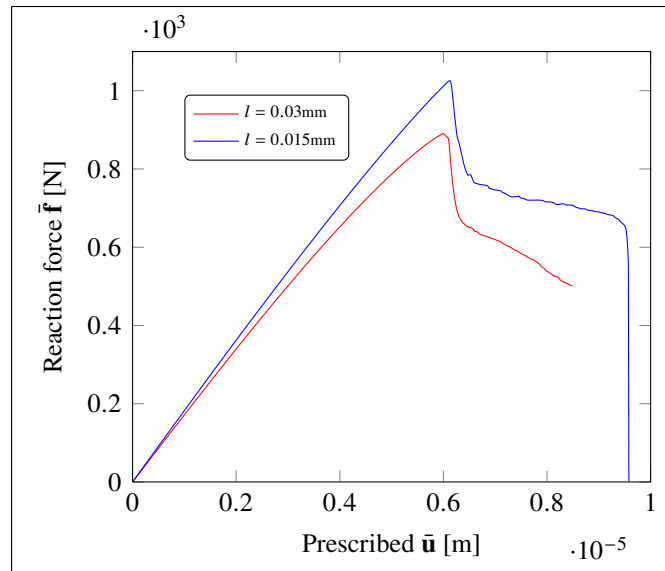Q4 elements: crack trajectory at the specific point of the curve in Figure (III-5)

Figure-A III-5   Load-displacement curve in the shear test of
sample containing 10406 Q4 elements

BIBLIOGRAPHY

Ambati, M., Gerasimov, T. & De Lorenzis, L. (2015a). Phase-field modeling of ductile fracture. *Computational Mechanics*, 55(5), 1017–1040. doi: 10.1007/s00466-015-1151-4.

Ambati, M., Gerasimov, T. & De Lorenzis, L. (2015b). A review on phase-field models of brittle fracture and a new fast hybrid formulation. *Computational Mechanics*, 55(2), 383–405. doi: 10.1007/s00466-014-1109-y.

Ambati, M., Kruse, R. & De Lorenzis, L. (2016). A phase-field model for ductile fracture at finite strains and its experimental verification. *Computational Mechanics*, 57(1), 149–167. doi: 10.1007/s00466-015-1225-3.

Amor, H., Marigo, J.-J. & Maurini, C. (2009). Regularized formulation of the variational brittle fracture with unilateral contact: Numerical experiments. *Journal of the Mechanics and Physics of Solids*, 57(8), 1209 - 1229. doi: http://dx.doi.org/10.1016/j.jmps.2009.04.011.

Badnava, H., Etemadi, E. & Msekh, M. A. (2017). A Phase Field Model for Rate-Dependent Ductile Fracture. *Metals*, 7(5). doi: 10.3390/met7050180.

Barenblatt, G. (1962). The Mathematical Theory of Equilibrium Cracks in Brittle Fracture (vol. 7, pp. 55-129). Elsevier. doi: https://doi.org/10.1016/S0065-2156(08)70121-2.

Begley, J. A. & Landes, J. D. (1972). The J Integral as a Fracture Criterion. *Fracture Toughness, Proceedings o f the 1971 National Symposium on Fracture Mechanics, Part II, ASTM STP 514*, pp. 1-20.

Besson, J. (2010). Continuum Models of Ductile Fracture: A Review. *International Journal of Damage Mechanics*, 19(1), 3-52. doi: 10.1177/1056789509103482.

Borden, M. J., Verhoosel, C. V., Scott, M. A., Hughes, T. J. & Landis, C. M. (2012). A phase-field description of dynamic brittle fracture. *Computer Methods in Applied Mechanics and Engineering*, 217-220, 77-95. doi: https://doi.org/10.1016/j.cma.2012.01.008.

Borden, M. J., Hughes, T. J., Landis, C. M. & Verhoosel, C. V. (2014). A higher-order phase-field model for brittle fracture: Formulation and analysis within the isogeometric analysis framework. *Computer Methods in Applied Mechanics and Engineering*, 273, 100 - 118. doi: http://dx.doi.org/10.1016/j.cma.2014.01.016.

Bourdin, B., Francfort, G. & Marigo, J.-J. (2000). Numerical experiments in revisited brittle fracture. *Journal of the Mechanics and Physics of Solids*, 48(4), 797 - 826. doi: http://dx.doi.org/10.1016/S0022-5096(99)00028-9.

Bourdin, B., Francfort, G. A. & Marigo, J.-J. (2008). The variational approach to fracture. *Journal of Elasticity*, 91(1-3), 5-148. doi: 10.1007/s10659-007-9107-3.

Braides, A. (1998). *Approximation of free-discontinuity problems* (ed. 1st ed. 1998.). Berlin, Germany: Springer.

de Souza Neto, E. A., Perić, D. & Owen, D. R. J. (2008a). The Finite Element Method in Quasi-Static Nonlinear Solid Mechanics. In *Computational Methods for Plasticity* (ch. 4, pp. 83-113). John Wiley Sons, Ltd. doi: https://doi.org/10.1002/9780470694626.ch4.

de Souza Neto, E. A., Perić, D. & Owen, D. R. J. (2008b). Plane Stress Plasticity. In *Computational Methods for Plasticity* (ch. 9, pp. 357-401). John Wiley Sons, Ltd. doi: https://doi.org/10.1002/9780470694626.ch9.

Dimitri, R., De Lorenzis, L., Wriggers, P. & Zavarise, G. (2014). NURBS- and T-spline-based isogeometric cohesive zone modeling of interface debonding. *Computational Mechanics*, 54(2), 369–388. doi: 10.1007/s00466-014-0991-7.

Dvorak, G. J. & Rao, M. (1976). Axisymmetric plasticity theory of fibrous composites. *International Journal of Engineering Science*, 14(4), 361-373.

Dvorak, G. J., Bahei-El-Din, Y. & Wafa, A. (1994). Implementation of the transformation field analysis for inelastic composite materials. *Computational Mechanics*, 14(3), 201-228. doi: 10.1007/BF00370073.

Francfort, G. & Marigo, J.-J. (1998). Revisiting brittle fracture as an energy minimization problem. *Journal of the Mechanics and Physics of Solids*, 46(8), 1319-1342. doi: https://doi.org/10.1016/S0022-5096(98)00034-9.

Gerasimov, T. & De Lorenzis, L. (2016). A line search assisted monolithic approach for phase-field computing of brittle fracture. *Computer Methods in Applied Mechanics and Engineering*, 312, 276-303. doi: https://doi.org/10.1016/j.cma.2015.12.017. Phase Field Approaches to Fracture.

Geuzaine, C. & Remacle, J.-F. (2009). Gmsh: A 3-D finite element mesh generator with built-in pre- and post-processing facilities. *International Journal for Numerical Methods in Engineering*, 79(11), 1309-1331. doi: https://doi.org/10.1002/nme.2579.

Griffith, A. A. & Taylor, G. I. (1921). VI. The phenomena of rupture and flow in solids. *Philosophical Transactions of the Royal Society of London. Series A, Containing Papers of a Mathematical or Physical Character*, 221(582-593), 163-198. doi: 10.1098/rsta.1921.0006.

Guennebaud, G., Jacob, B. et al. (2010). Eigen v3. Retrieved from: http://eigen.tuxfamily.org.

Gurson, A. L. (1977). Continuum Theory of Ductile Rupture by Void Nucleation and Growth: Part I -Yield Criteria and Flow Rules for Porous Ductile Media. *Journal of Engineering Materials and Technology*, 99(1), 2-15.

Heister, T., Wheeler, M. F. & Wick, T. (2015). A primal-dual active set method and predictor-corrector mesh adaptivity for computing fracture propagation using a phase-field approach. *Computer Methods in Applied Mechanics and Engineering*, 290, 466-495. doi: https://doi.org/10.1016/j.cma.2015.03.009.

Hill, R. (1963). Elastic properties of reinforced solids: some theoretical principles. *Journal of the Mechanics and Physics of Solids*, 11, 357–372. doi: 10.1016/0022-5096(63)90036-X.

Hill, R. (1972). On constitutive macro-variables for heterogeneous solids at finite strain. *Proceedings of the Royal Society of London, Series A*, 326, 131-147.

Irwin, G. R. (1956). Onset of Fast Crack Propagation in High Strength Steel and Aluminum Alloys. *Sagamore Research Conference Proceedings*, 2, 289–305.

Irwin, G. R. (1957). Analysis of Stresses and Strains Near the End of a Crack Traversing a Plate. *Journal of Applied Mechanics*, 24(3), 361-364. doi: 10.1115/1.4011547.

Karma, A., Kessler, D. A. & Levine, H. (2001). Phase-Field Model of Mode III Dynamic Fracture. *Phys. Rev. Lett.*, 87, 045501. doi: 10.1103/PhysRevLett.87.045501.

Kuhn, C. & Müller, R. (2010). A continuum phase field model for fracture. *Engineering Fracture Mechanics*, 77(18), 3625-3634. doi: https://doi.org/10.1016/j.engfracmech.2010.08.009. Computational Mechanics in Fracture and Damage: A Special Issue in Honor of Prof. Gross.

Kuhn, C., Schlüter, A. & Müller, R. (2015). On degradation functions in phase field fracture models. *Computational Materials Science*, 108, 374-384. doi: https://doi.org/10.1016/j.commatsci.2015.05.034. Selected Articles from Phase-field Method 2014 International Seminar.

Kuhn, C., Noll, T. & Müller, R. (2016). On phase field modeling of ductile fracture. *GAMM-Mitteilungen*, 39(1), 35-54. doi: https://doi.org/10.1002/gamm.201610003.

Mandel, J. (1971). Plasticité Classique et Viscoplasticité. CISM Lecture Notes No. 97. Springer, Udine.

Miehe, C., Welschinger, F. & Hofacker, M. (2010a). Thermodynamically consistent phase-field models of fracture: Variational principles and multi-field FE implementations. *International Journal for Numerical Methods in Engineering*, 83(10), 1273–1311. doi: 10.1002/nme.2861.

Miehe, C., Hofacker, M. & Welschinger, F. (2010b). A phase field model for rate-independent crack propagation: Robust algorithmic implementation based on operator splits. *Computer Methods in Applied Mechanics and Engineering*, 199(45), 2765-2778. doi: https://doi.org/10.1016/j.cma.2010.04.011.

Moës, N., Dolbow, J. & Belytschko, T. (1999). A finite element method for crack growth without remeshing. *International Journal for Numerical Methods in Engineering*, 46(1), 131–150. doi: 10.1002/(SICI)1097-0207(19990910)46:1<131::AID-NME726>3.0.CO;2-J.

Molnár, G. & Gravouil, A. (2017). 2D and 3D Abaqus implementation of a robust staggered phase-field solution for modeling brittle fracture. *Finite Elements in Analysis and Design*, 130, 27-38. doi: https://doi.org/10.1016/j.finel.2017.03.002.

Moës, N., Stolz, C., Bernard, P.-E. & Chevaugeon, N. (2011). A level set based model for damage growth: The thick level set approach. *International Journal for Numerical Methods in Engineering*, 86(3), 358-380. doi: https://doi.org/10.1002/nme.3069.

Msekh, M. A., Sargado, J. M., Jamshidian, M., Areias, P. M. & Rabczuk, T. (2015). Abaqus implementation of phase-field model for brittle fracture. *Computational Materials Science*, 96, 472-484. doi: https://doi.org/10.1016/j.commatsci.2014.05.071. Special Issue Polymeric Composites.

Ortiz, M. & Pandolfi, A. (1999). Finite-deformation irreversible cohesive elements for three-dimensional crack-propagation analysis. *International Journal for Numerical Methods in Engineering*, 44(9), 1267–1282. doi: 10.1002/(SICI)1097-0207(19990330)44:9<1267::AID-NME486>3.0.CO;2-7.

Pretti, G., Coombs, W. M. & Augarde, C. E. (2022). A displacement-controlled arc-length solution scheme. *Computers Structures*, 258, 106674. doi: https://doi.org/10.1016/j.compstruc.2021.106674.

Rice, J. R. (1968). A Path Independent Integral and the Approximate Analysis of Strain Concentration by Notches and Cracks. *Journal of Applied Mechanics*, 35(2), 379-386. doi: 10.1115/1.3601206.

Rice, J. & Sorensen, E. (1978). Continuing crack-tip deformation and fracture for plane-strain crack growth in elastic-plastic solids. *Journal of the Mechanics and Physics of Solids*, 26(3), 163 - 186. doi: http://dx.doi.org/10.1016/0022-5096(78)90007-8.

Simo, J. C., Oliver, J. & Armero, F. (1993). An analysis of strong discontinuities induced by strain-softening in rate-independent inelastic solids. *Computational Mechanics*, 12, 277-296.

Tvergaard, V. & Needleman, A. (1984). Analysis of the cup-cone fracture in a round tensile bar. *Acta Metallurgica*, 32(1), 157 - 169. doi: http://dx.doi.org/10.1016/0001-6160(84)90213-X.

Williams, M. L., Ellinger, G. A. et al. (1953). Investigation of structural failures of welded ships. *Welding Journal*, 32(10).

Wu, J.-Y., Nguyen, V. P., Nguyen, C. T., Sutula, D., Sinaie, S. & Bordas, S. P. (2020). Chapter One - Phase-field modeling of fracture (vol. 53, pp. 1-183). Elsevier. doi: https://doi.org/10.1016/bs.aams.2019.08.001.

Xu, X.-P. & Needleman, A. (1994). Numerical simulations of fast crack growth in brittle solids. *Journal of the Mechanics and Physics of Solids*, 42(9), 1397-1434. doi: https://doi.org/10.1016/0022-5096(94)90003-5.

Zienkiewicz, O., Taylor, R. & Fox, D. (2014). Chapter 1 - General Problems in Solid Mechanics and Nonlinearity. In Zienkiewicz, O., Taylor, R. & Fox, D. (Eds.), *The Finite Element Method for Solid and Structural Mechanics (Seventh Edition)* (ed. Seventh Edition, pp. 1-20). Oxford: Butterworth-Heinemann. doi: https://doi.org/10.1016/B978-1-85617-634-7.00001-6.